MECHANICAL CHARACTERIZATION OF HETEROGENEOUS HYPERELASTIC MEMBRANE USING INVERSE METHODS

By

S. M. RAKIBUR RAHMAN

Bachelor of Science in Aeronautical Engineering

Bangladesh University of Professionals

Dhaka, Bangladesh

2017

Submitted to the Faculty of the
Graduate College of the
Oklahoma State University
in partial fulfillment of
the requirements for
the Degree of
MASTER OF SCIENCE
December, 2021

MECHANICAL CHARACTERIZATION OF

HETEROGENEOUS HYPERELASTIC MEMBRANE

USING INVERSE METHODS

Thesis Approved:

Dr. Shuodao Wang

Thesis Adviser

Dr. Sandip Harimkar

Dr. Kaan Kalkan

ACKNOWLEDGEMENTS

Firstly, I would like to extend my deepest gratitude to my advisor Dr. Shuodao Wang for his continuous support and motivation. Without his guidance and persistent help, this thesis would not have been possible.

I would also like to acknowledge Dr. Sandip Harimkar and Dr. Kaan Kalkan as the committee members of this thesis, and I am thankful to them for their valuable comments on this thesis.

I must thank the Oklahoma Center for Advancements of Science and Technology (OCAST) for supporting this research.

Finally, I am extremely grateful to my parents, sister, and to my wife for providing me with support and continuous encouragement.

Name: S. M. RAKIBUR RAHMAN

Date of Degree: DECEMBER, 2021

Title of Study: MECHANICAL CHARACTERIZATION OF HETEROGENEOUS HYPERELASTIC MEMBRANE USING INVERSE METHODS

Major Field: MECHANICAL AND AEROSPACE ENGINEERING

Abstract: Many soft biological tissues are heterogeneous, having different properties at different locations. Characterizing these tissues is very important for virtually testing potential medical technologies or protocols. Some synthetic thin structures used in various manufacturing processes are also complex in material composition. Determination of the mechanical properties of these structures is critical for industrial production. These materials can undergo very large deformation in actual applications and their behavior is nonlinear. This makes their characterization difficult and there is a need for an efficient method. In this study, hyperelastic material properties of a heterogeneous synthetic flat membrane with two constituent materials are determined using two inverse methods. One method is the traditional Finite Element Model Updating Method and the other is based on machine learning using a deep neural network. Inverse modeling was done in moderate strain range (engineering strain up to 37 %) with the Neo-Hookean material model and in the large strain (engineering strain up to 93%) range using the Yeoh model. Both the inverse methods were found to have very good accuracy. Accuracy in the moderate strain range was slightly higher than that of the high strain range. For both strain range, the coefficient of determination values were very close to 1 for both the stress-strain curves and the work-energy curves, which indicates very good accuracy. The machine learning method was six orders of magnitude faster than the Finite Element Model Updating Method.

TABLE OF CONTENTS

Chapter Page

LIST OF TABLES

Table Page

LIST OF FIGURES

Figure Page

Figure Page

CHAPTER I

INTRODUCTION AND BACKGROUND

1.1 Introduction

Many soft biological tissues such as eardrums [1], skins [2], heart valves [3] are heterogeneous. Characterization of the physical properties of these tissues is challenging. Many bio-tissues are soft and complex and therefore, preparing testing bio-samples is very difficult. A limited number of bio-samples can't represent the properties of an entire tissue since tissue properties vary at different locations. It is desirable to obtain the bio-tissue properties in vivo because when they are removed from their bio-contexts, their properties change with time. Soft bio-tissues can undergo very large deformation in extreme conditions [4]. The tissues exhibit nonlinear behavior [5] which is difficult to characterize. Synthetic thin structures such as stretchable electronics [6], foam metals [7], and non-woven fabrics [8] have complex material compositions. For the optimization of industrial production processes, it's critical to obtain the mechanical properties of these heterogeneous thin products. They can also undergo large deformation [9] in actual applications. The linear elastic model is incapable of characterizing materials that undergo large deformation. Hyperelastic and viscoelastic models are required for this purpose.

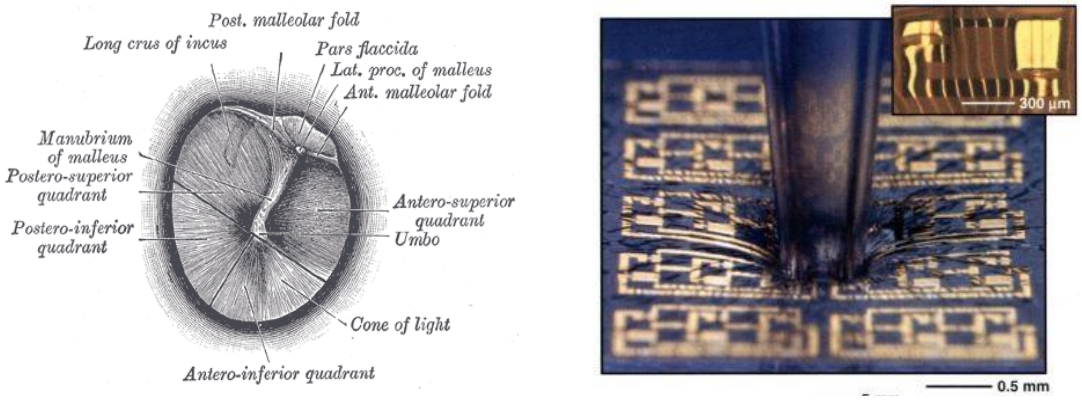

(a) (b)

Figure 1.1 (a) Tympanic membrane with various properties at various locations [10] (b) Stretchable silicon circuit in a wavy geometry, compressed in its center by a glass capillary tube (main) and wavy logic gate built with two transistors (top right inset) [6]

In this research, a combination of numerical simulation, theoretical study, and experimental validation was used to achieve the following specific objectives:

a) Develop an efficient computational framework to solve an inverse problem to determine the hyper-elastic mechanical properties of thin, flat, heterogeneous membranes based on full-field strain measurements.

b) Compare the accuracy and efficiency of the developed Machine Learning based inversed method to those of the traditional Finite Element Model Updating method.

c) Validate the framework on synthesized membranes consisting of elastomers of two different elastic moduli.

1.2 Background

1.2.1 Heterogeneous materials

Heterogeneous materials consist of significantly different and randomly distributed materials. Constituent heterogeneity, microstructural heterogeneity, or crystal structure heterogeneity can cause material heterogeneity. The domain can be of various sizes and geometry.

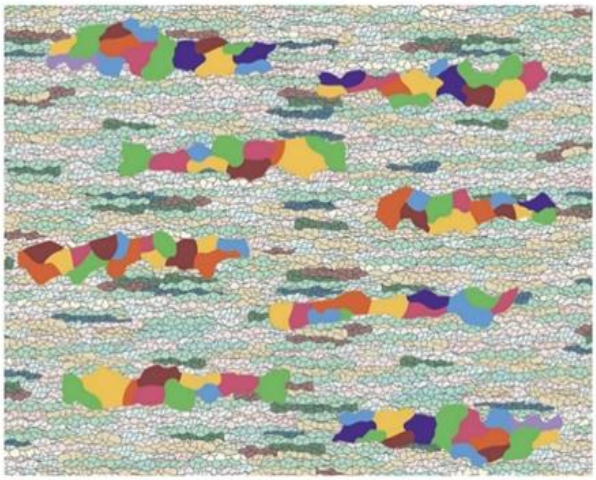

Figure 1.2 Schematics of a heterogeneous lamella structure [11]

1.2.2 Strain Measurement

A branch of new methods has emerged to measure soft materials deformation with the development of microscopic and electron microscope technology. In a scanning electron microscopy (SEM) system [12], a beam of electrons is produced with an electron gun. A path through the microscope within a vacuum is followed by the electron beam. Electrons and X-rays are ejected from the sample when the beam hits the sample. These X-rays, backscattered electrons, and secondary electrons are collected by detectors and are then converted into a signal that is converted to produce the final image. There are three functional parts of an atomic force microscopy (AFM) system [13]: a sharp tip mounted to a piezoelectric actuator, a micro-machined cantilever probe, and a position-sensitive photodetector. During operation, the sharp tip scans the surface of the sample. The light intensities on the photodetectors fluctuate while the tips move up and down with the profile of the surface. A Scanning tunneling microscope (STM) [14] is based on quantum tunneling. It consists of a metallic tip, which is brought very near to the surface of the sample to be examined, with applied voltage. Electrons are extracted from the surface by quantum tunneling when voltage is applied. An electrical current is created between the tip and the surface. When the tip lies on top of an atom,

tunneling occurs at very short distances. The position of the atoms of the metal surface can be deduced by drawing the current intensity versus the tip.

There are some limitations of the methods described above. AFM is limited to a very small area and relies on contact surface scanning. SEM is not possible for any in vitro/in vivo setup since it requires a conductive surface and a high-energy electron beam (tens of kV) to scan the surface. Sample preparation in the form of fixation, dehydration, and staining is required for SEM and STM, which can have a shrinking effect on bio-membranes resulting in dysfunction. The electron beam can cause damage to the biological samples Therefore, all kinds of electron microscopy are not the best option for biomaterials measurement [15].

Non-contact measurement techniques such as the conventional laser confocal microscopy for 3D profilometry [16] are not suitable for real-time measurements when fast evolution under high strain-rate loading is involved, since it requires the acquisition of a set of images and takes a relatively long time. Spinning disk confocal microscopy [17] is not fast enough for the investigation of the hyper-elastic behavior of biomaterials under large deformation. Reflected light confocal microscopy [18] also suffers from low real-time imaging speed.

Digital image correlation (DIC) is another widely used technique in the field of mechanics [19–22]. During the implementation of the 2D DIC [23] method, the first step is to define a region of interest (ROI) in the reference image. This region is further divided into evenly spaced grids as shown in Figure 1.3(a). The displacements are computed at each point of the virtual grids. Full-field deformation (Figure 1.3(b)) is obtained by computing displacement at each point of the virtual grid. In DIC, the same points or pixels are tracked from the two images recorded before and after deformation as schematically illustrated in Figure 1.4. To compute the displacements of point P, a reference subset centered at point P (x_0, y_0) from the reference image is used to track its corresponding location in the deformed image. A square subset is chosen rather than an individual

pixel because a subset comprising a wider variation in gray levels can distinguish itself from other subsets.

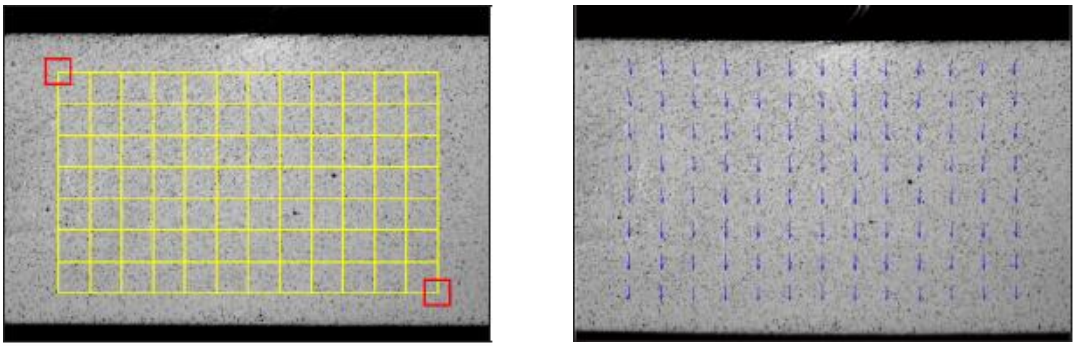

(a) (b)

Figure 1.3 (a) Region of interest divided into grids. Intersection points on the grid denote points in which displacement will be calculated, the red square is the subset used for tracking motion of centerpoint (b) calculated displacement vectors [23]

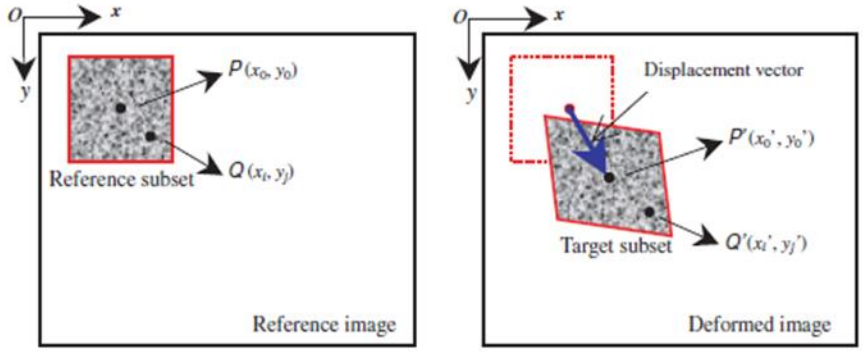

Figure 1.4 Reference subset before deformation (left) and a target subset after deformation (right) [23]

A cross-correlation (CC) criterion or sum-squared difference (SSD) correlation criterion is predefined to determine the similarity degree between the reference subset and the deformed subset. Once the correlation coefficient extremum, which is the peak position of the distribution of correlation coefficient is detected, the deformed subset position is determined. The in-plane

displacement vector at point P is found from the differences in the positions of the reference subset center and the target subset center.

Only in-plane deformation measurement of the planar object surface can be captured by 2D DIC, To overcome this limitation 3D DIC was developed by applying the principle of binocular stereo-vision [24,25]. The digital volume correlation (DVC) [26] method is another direct 3D extension of a 2D DIC method that can show the internal deformation field of solid objects by tracking the movement of a volume unit within digital image volumes of the sample.

1.2.3 Inverse methods based on full-field measurements

A system response can be predicted with a reliable model and known input parameters. The type of problem aiming at finding system response for given input parameters is referred to as a direct problem. A problem is an inverse [27] when it deals with the estimation of the parameters based on a given model and system response. Full-field displacement/strain measurement techniques such as Digital Image Correlation and Digital Volume Correlation have paved the way for various inverse identification methods [28] for the characterization of heterogeneous materials constituents.

Finite element model updating [29,30] is the most widely used inverse strategy. This method iteratively updates the material parameters input into the finite element model based on the comparison of the corresponding output data after forward analysis (typically displacement or strain fields) and their experimental counterparts. The aim is to identify the set of parameters that provide the best match between numerical outputs and real behavior captured through experiments. FEMU can be utilized to determine the distribution of properties in materials with heterogeneous stress/strain fields. One of the benefits of the FEMU method is the fact that full-field measurements on the whole domain are not required [31] and therefore, it can carry out parameter identification using partial knowledge on the displacement data. Inverse solutions within a smaller region of interests are normally preferred as these would be more stable and generate less discretization error.

Moreover, material models with complex geometries and boundary conditions can be characterized by taking the advantage of finite element simulation capabilities. An inverse technique was developed by Wang et al [32] for identifying viscoelastic adhesive interfacial parameters relying on damage state at the interface. To record failure positions of interfacial area, deformation images were recorded at the surface of the specimen. An inverse strategy was proposed by Fedele et al. [33] for estimating mechanical parameters of a cohesive law of an adhesive layer using full-field displacement data supplied by DIC.deformation measurement of the planar object surface can be captured by 2D DIC.

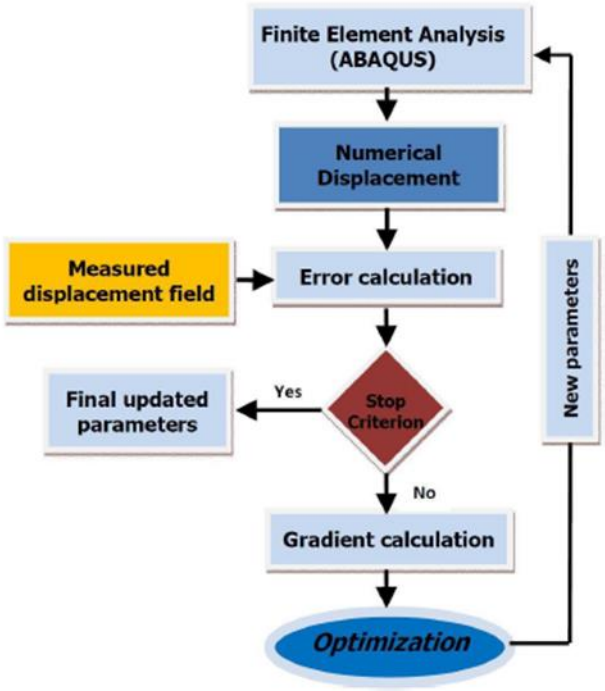

Figure 1.5 Finite Element Model Updating algorithm [34]

The constitutive equation gap method (CEGM) [35] is also called an Error in the Constitutive Equation. The principle of CEGM is to minimize the difference between a statically admissible stress field and the stress field calculated from a measured displacement field and a chosen constitutive model. The first step is to define an initial set of material parameters, then the statically

admissible stress field with this initial set of material parameters will be determined. Then an objective function is evaluated, which is based on the error of the two stress fields. An optimization method will keep optimizing the set of material parameters until the value of the objective function reaches a given threshold. After that, the statically admissible stress field is updated following a user-defined criterion. In some cases, the FE model is adopted, and the determination of the statically admissible stress field is performed before the minimization of the objective function. The whole process is repeated until the convergence criterion is reached, which is calculated by comparing the stress in the current and previous iteration. This method has been applied to study heterogeneous materials [36], anisotropic elasticity [37], plasticity [38], and damage [39]

Grédiac proposed the Virtual Fields Method (VFM) in 1989 [40]. The key elements in VFM are the Principle of Virtual Work and a suitable choice of virtual fields. For a solid body in the absence of body-forces and under infinitesimal small displacements, the Principle of Virtual Work is that the internal virtual work must equal the external virtual work performed by the external forces. This method has been used to determine stiffness constants of orthotropic laminated composites, nonlinear shear behavior of composites [41], detection of heterogeneities [42] in functionally graded materials, Promma et al [43] identified Mooney model constitutive parameters retrieved from a multiaxial mechanical test using VFM.

The FEMU has some special features which make it the most widespread method among all the above-mentioned identification techniques. The computation time can be reduced in the identification process as this method does not require full-field measurement data on the whole domain. When specimens with complex geometries and boundary conditions are to be categorized, this technique also benefits from the robustness of the finite element method. However, this method is computationally expensive because of time-consuming finite element calculations, especially when dealing with 3D models, which is the main drawback of this method. The VFM requires full-

field data within the domain and is also very sensitive to noise. This method is not iterative, which immediately brings a limitation that this method does not follow any regularization.

With the increasing amount of data availability, powerful GPUs, and the development of new algorithms, machine learning has revolutionized several fields. Data generated by FEA is noise-free. Several studies have used virtually generated FEA data [44,45] to train learning algorithms. A machine learning approach was proposed by Lorente et al [46] to model the mechanical behavior of the liver during real-time breathing. Several regression models were trained. External displacement and elasticity parameters were used as input and the FEM-based nodal displacements were used as output. Deep learning has been shown to have the ability to simulate hyperelastic-material in real-time [47]. Wang et al. [48] used Gappy proper orthogonal decomposition (POD) for inverse material characterization. POD is a model order reduction method. The geometry of the structure, the boundary conditions, and the partial-field response measurements from a nondestructive testing procedure was the input. Response of the structure under the testing conditions is calculated based on an initial guess of material property distribution by the forward analysis procedure. Then POD modes were calculated using full-field structural responses. The full-field response was updated using Gappy POD. The updated response was compared with data generated by physics-based simulation. The results were accurate for both static and dynamic modes. The procedure was computationally efficient compared to the traditional mathematical derivation. The expense of the inverse characterization procedure, which includes the training of the POD modes, was comparable to less than 40 standard finite element analyses for the simulated examples. The inversion procedure was equivalent to a single standard finite element analysis after the development of the POD modes. Artificial neural networks have also been used to model material behavior [49].

1.2.4 Hyperelastic models

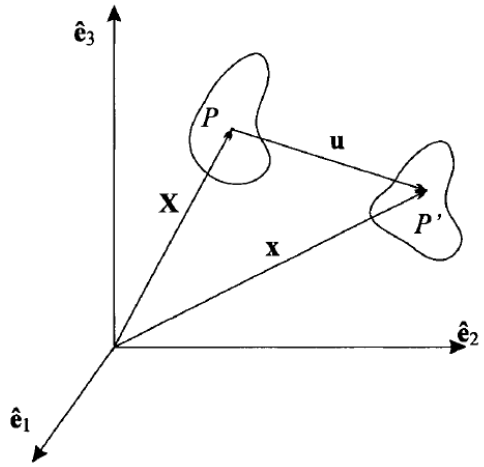

Figure 1.6 Position vectors and displacement vector in a cartesian coordinate system [50]

A brief discussion of some basics of continuum mechanics is helpful at this point for understanding the formulation of hyperelastic models. A given point, P, in a body is defined as having the reference position vector $\mathbf{X} = X_i\hat{\mathbf{e}}_\mathbf{i}$. Following a body deformation and/or motion, the new position of point P is defined by point P' which has the current position vector $\mathbf{x} = x_i\hat{\mathbf{e}}_\mathbf{i}$. The reference position vector, X, and the current position vector, x, are related by the displacement vector, u, such that

$$x_i = X_i + u_i \tag{1.1}$$

Indicial form of vectors, such as X_i or tensors, such as F_{ij} is simply a different way of expressing their equivalent bold font style, matrix form, **X** and **F**, respectively. The differential form of equation (1.1) can be reduced to

$$dx_i = \frac{\partial x_i}{\partial X_j} dX_j = F_{ij} dX_j \tag{1.2}$$

where Fij, here in indicial form, is commonly known as the deformation gradient tensor, or simply the deformation gradient, F, in matrix form. The right Cauchy-Green tensor, C, is obtained from the deformation gradient, such that

$$C_{ij} = F_{mi}F_{mj} \tag{1.3}$$

or in matrix form,

$$\mathbf{C} = \mathbf{F^T}.\mathbf{F} \tag{1.4}$$

We define stretch ratio, λ, for a one-dimensional element of reference length L_0, and current length L, such that

$$\lambda = \frac{L}{L_0} \tag{1.5}$$

The various types of strain used in this research are tabulated below:

Table 1.1 Different strain measures used in this study

Engineering strain	$\varepsilon_{eng} = \lambda - 1$
True strain	$\varepsilon_{true} = 1 - \frac{1}{\lambda}$
Logarithmic strain	$\varepsilon_{Log} = \ln\lambda$
Lagrangian strain	$\varepsilon_{Lag} = \frac{1}{2}(\lambda^2 - 1)$

The strain invariant can be defined from right Cauchy-Green tensor **C**, such that they are independent of the coordinate orientation.

$$I_1 = \lambda_1^2 + \lambda_2^2 + \lambda_3^2 = \mathrm{tr}(\mathbf{C}) \tag{1.6}$$

$$I_2 = \lambda_1^2\lambda_2^2 + \lambda_2^2\lambda_3^2 + \lambda_3^2\lambda_1^2 = \frac{1}{2}(I_1^2 - \mathrm{tr}(\mathbf{C}^2)) \tag{1.7}$$

$$I_3 = \lambda_1^2\lambda_2^2\lambda_3^2 = J^2 = \det(\mathbf{C}) \tag{1.8}$$

J is equal to 1 for incompressible materials. The hyperelastic constitutive behavior of a material is derived from strain energy function [49] 'W' which is a function of three invariants.

$$W = f(I_1, I_2, I_3) \tag{1.9}$$

A brief description of the hyperelastic models considered in this study are given below:

Mooney-Rivlin model

This is a phenomenological model with two parameters. It is suitable for moderately large strains in shear and uniaxial deformation [51,52]. However, it is incapable of capturing the upturn in the typical S shape of hyperelastic materials. The strain energy density of this model has the following form

$$W = C_{10}(I_1 - 3) + C_{01}(I_2 - 3) \tag{1.10}$$

Neo Hookean model

This model is obtained by setting C_{01}= 0 in the Mooney-Rivlin model. This model is suitable for small strains. It is simple to use since it has only one parameter. The strain energy density of this model has the following form:

$$W = C_{10}(I_1 - 3) \tag{1.11}$$

Yeoh

This phenomenological model [53] has the form of a third-order polynomial and is based only on the first invariant. Various modes of deformation can be simulated using this model with limited data [54]. This model is suitable for large strains. The strain energy density of this model has the following form:

$$W = \sum_{i=1}^{3} C_{i0}(I_1 - 3) \tag{1.12}$$

Ogden

This model [55] was proposed by Ogden in 1972. Instead of invariants, this model is based on principal stretches. This model can capture the full S shape of hyperelastic materials. The strain energy density of this model has the following form:

$$W = \sum_{i=1}^{N} \frac{2\mu_i}{\alpha_i^2} (\lambda_1^{\alpha_i} + \lambda_2^{\alpha_i} + \lambda_3^{\alpha_i}) \tag{1.13}$$

Arruda Boyce

This model [56] is based on a molecular chain network and is also called the Arruda Boyce 8-chain model. It is based on the first invariant and has the following form of strain energy density:

$$W = \mu \sum_{i=1}^{5} \frac{C_i}{\lambda_m^{2i-2}} (I_1^i - 3^i) \tag{1.14}$$

Shahzad et al [54] used hyperelastic models to characterize an indigenously developed rubber. Uniaxial, equi-biaxial, planar shear, and volumetric tests were conducted. They considered Mooney-Rivlin, Neo-Hookean, Yeoh, Ogden, and Arruda Boyce models. Yeoh model was found to match experimental stress-strain data better than other models at both small and large strain values. Vlad et al [57] characterized PDMS-based silicone elastomer films. Parameters of Mooney Rivlin, Ogden (N=2), Neo Hookean, Yeoh, Arruda Boyce, and Van der Waals model were determined by Abaqus from experimental stress-strain data. FEM simulations were performed to validate uniaxial tension data Mooney Rivlin, Yeoh, and Ogden models were found to have good accuracy. Ribeiro et al [58] performed the biaxial test on PDMS samples at different speeds. DIC was used to measure the displacement field and was found to be well suited for hyperelastic material analysis. Mooney Rivlin, Yeoh, and Ogden models were used for conducting numerical simulations. Yeoh model was found to be the most accurate after Comparison of FEM displacement field with that obtained from DIC. Kim et al [59] measured the nonlinear mechanical properties of

PDMS. Cyclic uniaxial tension and single-pull-to failure tension test were performed. Parameters of Neo-Hookean, second-order Ogden, and third-order Mooney models were computed. All models showed a good fit in the small strain region. However, only the second-order Ogden model was suitable for nonlinear, large strain regions. Tobajas et al [60] determined hyperelastic model parameter for simulation of Exxonmobil manufactured Santoprene 101-73 material. Uniaxial stress-strain and strain energy density data were supplied by the manufacturer. Mooney-Rivlin, Neo-Hookean, Ogden, Gent-Thomas, Yeoh, and Arruda Boyce models were considered. Mooney-Rivlin and Yeoh models were found to have superior accuracy over other models. The study conducted by Esmail et al [61] aimed at characterizing hyperelastic material based on uniaxial test only. The material characterized was a layer of chloroprene rubber. Mooney-Rivlin, Polynomial, Neo-Hookean, Yeoh, and Ogden models were used. Polynomial, Ogden, and Yeoh models were found to be convenient for fitting the hyperelastic behavior. Martins et al [62] studied the nonlinear mechanical behavior of silicone rubber and soft tissues subjected to uniaxial tension. They analyzed seven hyperelastic material models: Mooney-Rivlin, Yeoh, Humprey, Ogden, Neo-Hookean, Martins, and Veronda. Yeoh, Ogden, and Martins models produced the best results. Liu et al [63] investigated the nonlinear behavior of silica-filled and the Kevlar-filled thin rubber sheets under quasi-static uniaxial tension test. Four models were considered: original Neo-Hookean, extended or generalized Neo-Hookean, Mooney-Rivlin, and Ogden models. The Second-order Rivlin model and Ogden models were found to fit experimental data better. Thanakhun et al [64] studied PDMS material models for eco-friendly anti-fouling surfaces. Uniaxial tension test and punch shear test were conducted, and the following models were considered: Neo-Hookean, Mooney-Rivlin 3 and 5 parameters, Ogden (1, 2, 3 terms), Yeoh (1st, 2nd, 3rd order) and Arruda-Boyce material models. Yeoh 3rd order model was found to be most accurate in simulating both the uniaxial tension and shear loading. Huri et al [65] studied hyperelastic material models for finite element analysis of rubberlike materials. Uniaxial compression test was performed and material constants were

determined using curve fitting in ANSYS. Three term Yeoh model outperformed two term Mooney-Rivlin model.

1.2.5 Adopted methodologies

2D digital image correlation has been used in this study to obtain full-field strains. For inverse modeling, finite element model updating has been used. and a machine learning algorithm is integrated with the FEA. Neo-Hookean, Mooney-Rivlin, Ogden (N=1), and Arruda Boyce models are considered for inverse modeling in moderate strain range. Yeoh and Ogden (N=2) models are considered for inverse modeling in large strain range.

CHAPTER II

METHODOLOGY

2.1 Specimen Fabrication:

Polydimethylsiloxane (PDMS) [66] Sylgard 184 was processed to make specimens of different stiffnesses. PDMS can be considered incompressible [67] Molds of specified geometries were created using a CNC milling machine.

Figure 2.1 CNC milled mold for making specimens

The PDMS base and curing agent were mixed at a chosen weight ratio. The mixture was degassed in a vacuum chamber till the point when there were no bubbles. The mixture was cast into the mold. Specimens were then cured in an oven at 100°C. Curing time [68] and mixing ratio [69] was varied to create materials with different stiffnesses. First material was cast in the mold and cured. Then it was cut in half and second material was cast in the mold and cured. Heterogeneous specimens with strong material interfaces were obtained through this method. This is important since the specimens

were subjected to high strain during the uniaxial tension test. Three homogeneous specimens of each constituent and one heterogeneous specimen were cut. The specimen fabrication process is shown in Figure 2.2. The heterogeneous specimens had dimensions 60mm×15mm. M1 had a thickness of 1.09 mm and M2 had a thickness of 1.06 mm. The heterogeneous specimens had dimensions of 30mm×5mm and thickness was about 1mm. The three homogeneous specimens made of material 1 are labeled M1_1, M1_2, and M1_3. The three homogeneous specimens made of material 2 are labeled M2_1, M2_2, and M2_3.

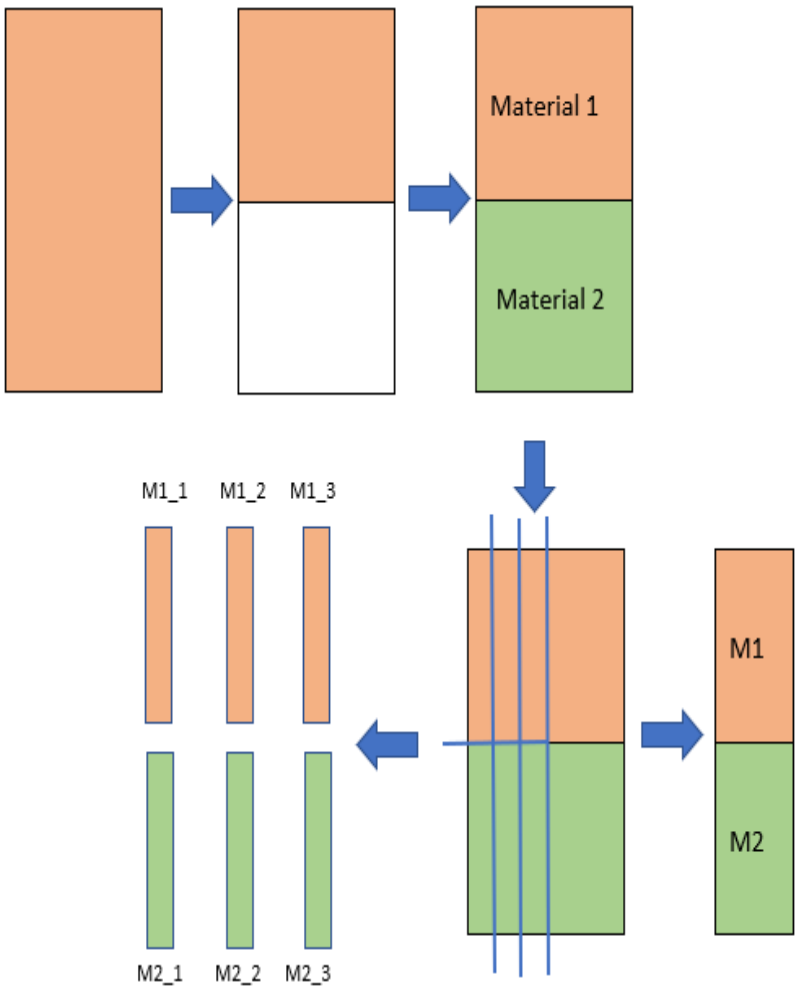

Figure 2.2 Specimen fabrication

Five heterogeneous specimens were prepared and tested to validate the computational framework. Table 2.1 shows young's modulus of the two constituents of the five specimens. Young's modulus were calculated using 0-5% true stress-true strain data.

Table 2.1 Youngs Modulus (MPa) of the constituents of five 1×2 pattern specimens

	Specimen 1	Specimen 2	Specimen 3	Specimen 4	Specimen 5
M1	2.02 ± 0.01	1.10 ± 0.02	2.21 ± 0.03	1.79 ± 0.02	1.09 ± 0.04
M2	1.12 ± 0.05	1.95 ± 0.01	1.69 ± 0.02	1.20 ± 0.01	1.90 ± 0.02

After the specimens were fabricated, they were subjected to uniaxial testing.

2.2 Uniaxial testing:

An Instron 5942 system was used to perform tensile tests. Figure 2.3 shows the testing system.

Figure 2.3 Testing setup

A Nikon D5 camera (Tamron AF 90mm f/2.8 Di SP AF/MF 1:1 Macro Lens), with a resolution of 3840×2160 pixels, was used to record videos during the tensile test. The videos were converted into images in MATLAB, where each image corresponded to a specific load. A lamp was used to increase the contrast of the images.

2.2.1 Homogeneous specimen:

Three homogeneous specimens of each constituent of the heterogeneous specimen were tested. A cross-section of each specimen was entered in the software (Bluehill) associated with the testing system. Engineering stress was calculated by the system at specified times steps, which is load divided by the initial cross-sectional area. This was used directly in the analysis. However, the engineering strain data obtained from the system couldn't be used since it was based on grip displacement and ignored the effects of slippage. To get an accurate stress-strain curve, the engineering strain was calculated from markers. Two lines, separated by 10mm distance, were marked in the samples. Figure 2.4 shows a homogeneous specimen in the initial and stretched condition.

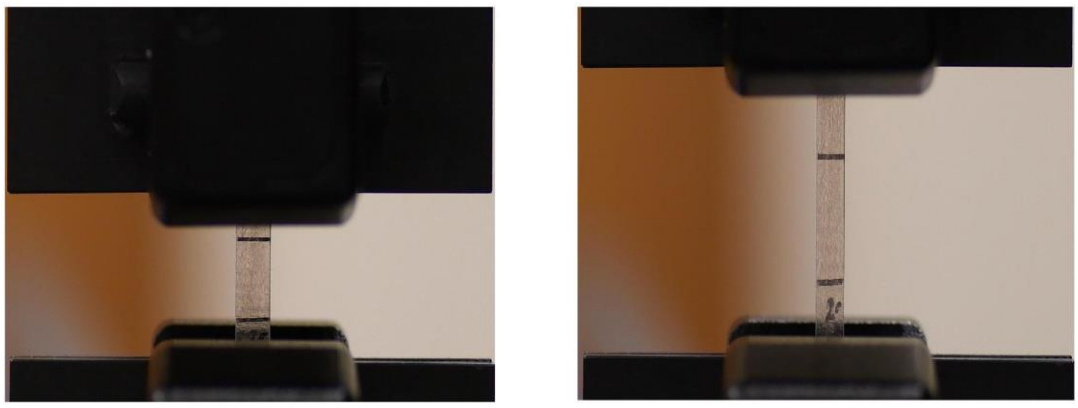

(a) (b)

Figure 2.4 A homogeneous specimen during uniaxial testing (a) Initial and (b) Stretched

Due to elongation number of pixels between the markers increased. The number of pixels between the lines was determined by a MATLAB program from images corresponding to different strain levels during the experiment. Pixels between markers in the first image were subtracted from the pixels between markers in the current image. The value was divided by pixels between markers in the first image and the engineering strain corresponding to the current image was obtained. The knurled grip was used in this research to minimize slip. Engineering stress-strain data was entered in the evaluate option in Abaqus. Several hyperelastic models can be fit to experimental data using this option.

2.2.2 Heterogeneous specimen

A random speckle pattern was generated using airbrush spraying on the heterogeneous specimens. Figure 2.5(a) shows a speckle pattern for one of the samples in this study, clamping boundary, and region of interest for DIC analysis.

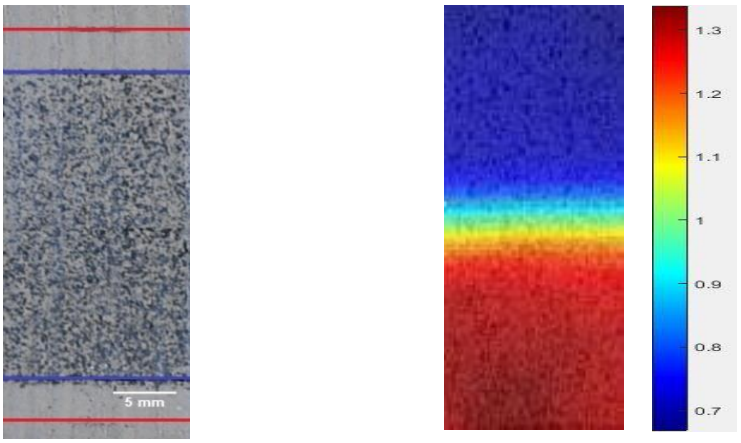

Figure 2.5 (a) Fabricated 1×2 heterogeneous specimen with DIC Region of Interest (blue lines) and clamping boundaries (red lines) (b) Full-field Lagrangian strain distribution obtained by 2D-DIC

The DIC analysis was done in the MATLAB open-source software Ncorr. The full-field strain distribution obtained from DIC analysis is shown in Figure 2.5(b).

For calibrating hyperelastic model parameters using engineering strain-engineering stress data, a strain range is needed. Since the model parameters are obtained from curve fitting, they vary with the strain range used to calibrate them. For example, calibrated parameters obtained from 0-25% stress-strain data are different from those obtained from 0-35% stress-strain data. Therefore, a strain range must be defined for each material of the heterogeneous specimen, which will be used to calibrate the hyperelastic model parameters. The maximum strain in this range is defined as the calibration strain in this study. Calibration strain for M1 and M2 are selected as the strain corresponding to the top and bottom boundary respectively of the region of interest. In Figure 2.5(b) Lagrangian strain values corresponding to the top and bottom boundaries are 0.7 and 1.3 respectively. By converting these values to engineering strain, we get calibration strain 0.55 (or 55%) for M1 and 0.9 (or 90%) for M2.

A high-quality speckle pattern is very important to get accurate DIC results. A good speckle pattern has high contrast, randomness, isotropy, and stability [70]. Figure 2.6 (a) shows grayscale distribution of the speckle pattern which shows the utilization of a wide spectrum of grayscale values and therefore, high contrast.

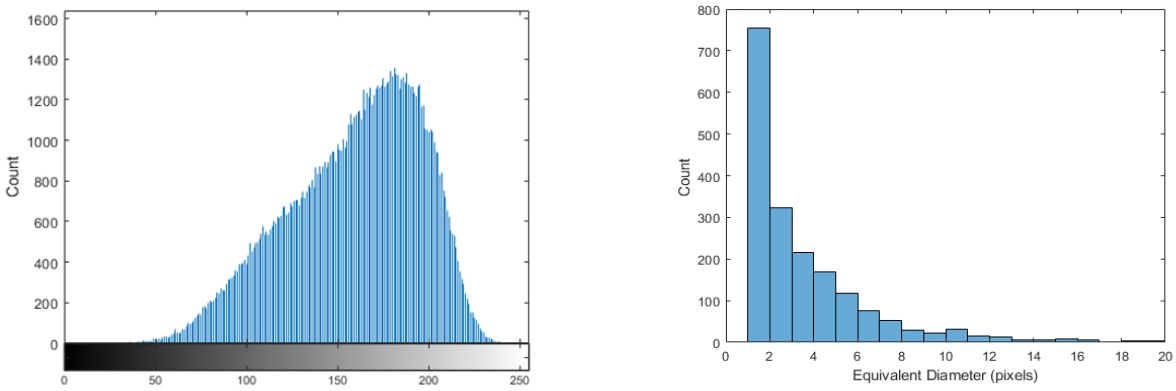

(a) (b)

Figure 2.6 (a) Grayscale distribution of speckle pattern (b) The distribution of the equivalent diameter of the speckle particles

The pattern is non-periodic and non-repetitive which indicates randomness. There is no visible directionality and it tightly adhered to the sample surface during experiments. Pan et al [71] proposed a global parameter, named mean intensity gradient (MIG) to assess the quality of speckle pattern. The parameter is defined as:

$$\mathrm{MIG} = \sum_{i=1}^{W}\sum_{j=1}^{H}\left|\nabla f(\mathbf{x}_{ij})\right| / (W \times H) \tag{2.1}$$

Where W and H are the image width and height in pixels, and

$$\left|\nabla f(x_{ij})\right| = \sqrt{f_x(\mathbf{x}_{ij})^2 + f_y(\mathbf{x}_{ij})^2} \tag{2.2}$$

$f_x(\mathbf{x}_{ij})$ and $f_y(\mathbf{x}_{ij})$ are the directional intensity derivatives in the x and y-direction.

It was shown that mean bias error and standard deviation error are smaller for speckle patterns having larger MIG values. In their study, they analyzed five speckle patterns and corresponding MIG values were: 34.64, 21.51,20.03,12.34, and 9.03. For the reference images of the five samples in this study, computed MIG values were on average 26. This indicates a good speckle pattern.

Choosing a proper subset size is another critical aspect of DIC analysis. Figure 2.6 (b) shows particle size distribution. most particles have an equivalent diameter of 1-5 pixels. And after averaging all the particles, an average diameter size was obtained in this ROI of 3.8 pixels. Following the work of Lecompte et al. [72] subset size was chosen to be 15 × 15 pixels in this study.

Figure 2.7 shows Load vs extension curve of the five 1×2 pattern specimens.

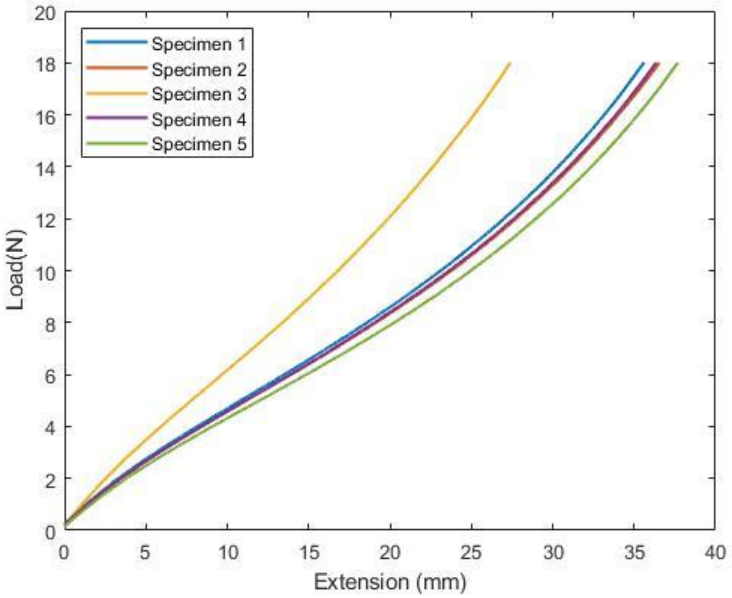

Figure 2.7 Load vs extension curves of five specimens

The curves have the typical S shape of hyperelastic materials. For inverse modeling in moderate strain range, the maximum load considered was 5N. For inverse modeling in large strain range, the maximum load considered was 18N.

2.3 Finite Element Model Updating:

Figure 2.8 Boundary conditions of the FEA model

A 2D plane stress model was used in Abaqus to model the heterogeneous specimens. Figure 2.8 shows the boundary conditions of the model. A mesh convergence study was conducted to determine the proper element size. M1 and M2 were defined according to Yeoh model parameter obtained for specimen 1 (Table 4.3, Page 50). 18N load was applied to the model, which is the maximum load applied to the specimens in this research, and the maximum strain was recorded for a various number of elements. A model with 600 elements was selected based on mesh convergence (Figure 2.9).

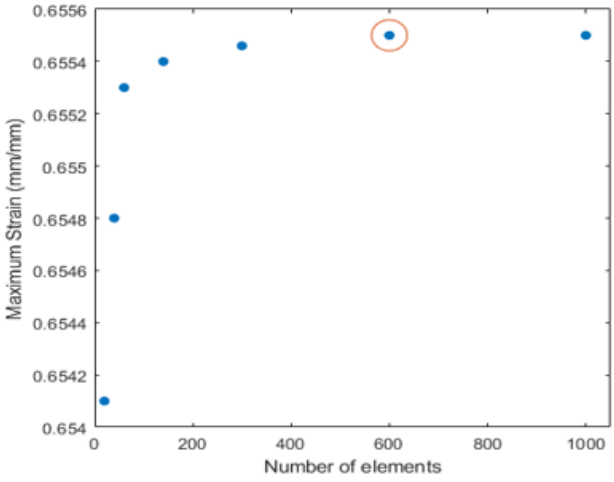

Figure 2.9 Mesh convergence

When more than one strain field was used for inverse modeling, multiple instances of the same model were created. Then different instances were assigned different loads. Figure 2.10 shows logarithmic strain distribution in y-direction obtained from an Abaqus simulation where five different loads (2N, 6N, 10N, 14N, and 18N) were applied to the instances.

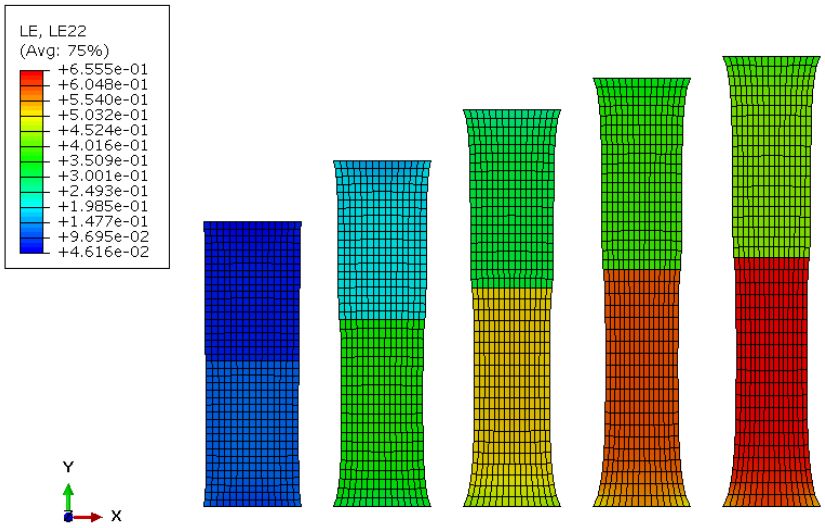

Figure 2.10 Logarithmic strain distribution in Abaqus simulation

The inverse modeling process was done with SIMULIA software Isight. The flowchart of the process is shown in Figure 2.11.

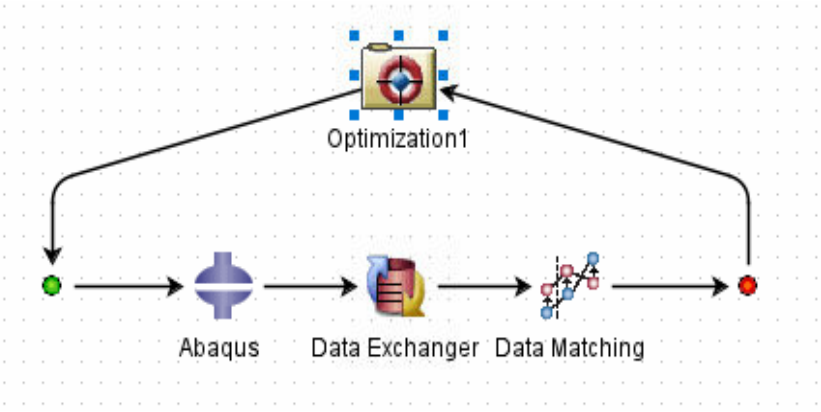

Figure 2.11 Isight optimization process

Abaqus: In this component, two files were read. One is the .inp file, which contains all the information to run the model. During the inverse modeling process, the material parameters are updated by the optimization algorithm in this file. Another file is the .odb file, which is generated after running the Abaqus model. This file contains the simulation results. From this file logarithmic strain values at selected nodes were obtained to be used later for comparing with the target strain values.

Data Exchanger: This component allows writing the value of a parameter into a file. A user can define options for handling structured data (e.g. tables of numbers, vectors, name/value lists, etc).

Data Matching: The target strain distribution is given within this component, which is matched with the strain distribution obtained from the simulation. This component provides input support for numerical array parameters generated upstream in the workflow. It also provides output support for error measures such as the sum of absolute difference, the sum of the squared difference, etc. This error information is then supplied to the optimization component.

Optimization: The optimization process in Isight can optimize material parameters to fit specified objectives. Many algorithms are available. After some trials, the Downhill Simplex algorithm was found to yield better results compared to other algorithms. An Intel® Core™ i5-6400 CPU was used to perform Finite element model updating (FEMU) analysis. Obtaining a mean square error less than 10^{-4} was the optimization objective.

2.4 Machine Learning:

The architecture of the deep neural network adopted in this study is shown in Figure 2.12.

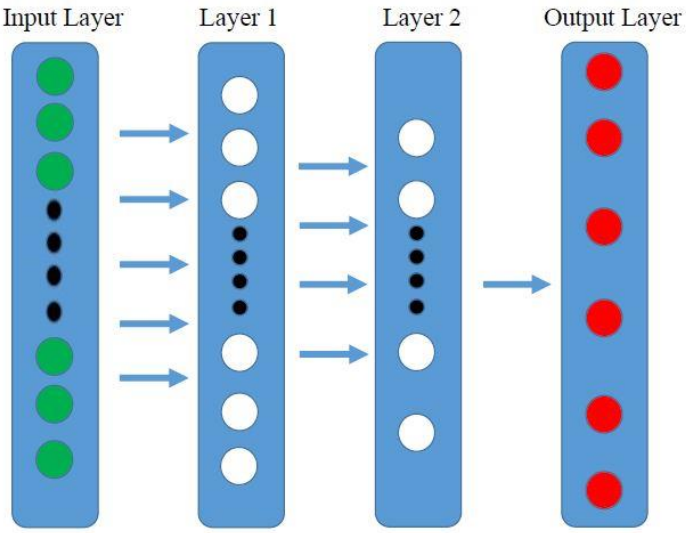

Figure 2.12 Architecture of the deep neural network

The strain of the selected elements in the specimen was used as the input. The input was mapped to a vector and fed into the network. The target parameters were estimated in the output layer. The network consists of two linear hidden layers before the output. 600 neurons were used in Layer 1 and 200 neurons in Layer 2. Mean squared error (MSE) was used as a loss function. The training time varies with network structure; training data amount; the resolution of the data and computer hardware. The neuron learning rate decayed with a factor of 0.95 for every 10,000 epochs in the training process to allow adjustments to improve the network-data fitting. The neuron parameters were updated automatically during training to minimize the MSE loss to ensure that the network produces accurate parameter predictions. The network was built and tested using NVIDIA GTX 750 ti graphic card with 640 CUDA cores. Once the network was developed and fully trained, it only took 1 millisecond to generate the required output for any new input (strain distribution) obtained from FEA-generated data or DIC experiments.

2.5 Determination of Fitting Accuracy

The fitting accuracy of the hyperelastic models is determined by calculating the coefficient of determination, denoted by R^2. It can have a value between 0 and 1. An R^2 value of 1 indicates a perfect fit. Considering a data set that has n values $y_1 \ldots y_n$. , each associated with a predicted value $f_1, \ldots f_n$. Mean of the observed data

$$\bar{y} = \frac{1}{n}\sum_{i=1}^{n} y_i \tag{2.3}$$

The sum of squares of residuals is calculated as

$$SS_{res} = \sum_{i}^{n} (y_i - f_i)^2 \tag{2.4}$$

The total sum of squares is calculated as

$$SS_{tot} = \sum_{i=1}^{n} (y_i - \bar{y})^2 \tag{2.5}$$

Then coefficient of determination can be calculated from the following equation

$$R^2 = 1 - \frac{SS_{res}}{SS_{tot}} \tag{2.6}$$

CHAPTER III

INVERSE MODELING IN MODERATE STRAIN RANGE

3.1 Model Selection

We define moderate strain as the strain level when the stress-strain curve has just become non-linear, so young's modulus is not sufficient to characterize the material. As described in section 2.2.2, for moderate strain range, 5N was the maximum load considered. Table 3.1 shows Calibration strain (%) obtained from full-field strain distribution corresponding to 5N load

Table 3.1 Calibration strain (%) obtained from full-field strain distribution corresponding to 5N load

Specimen 1		Specimen 2		Specimen 3		Specimen 4		Specimen 5	
M1	M2	M1	M2	M1	M2	M1	M2	M1	M2
17	36	35	19	15	22	20	35	37	20

Based on the literature review Neo-Hookean, Ogden(N=1), Mooney-Rivlin, and Arruda Boyce models were considered. Figure 3.1 shows how they fit the experimental data of one of the materials in this study (M1_1, Specimen 1).

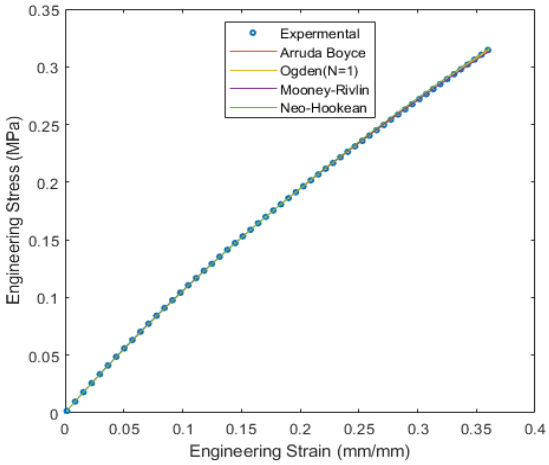

Figure 3.1 Neo-Hookean, Ogden(N=1), Mooney-Rivlin and Arruda-Boyce model fit to experimental data

Table 3.2 Model Parameters

Neo-Hookean	Mooney-Rivlin	Ogden(N=1)	Arruda Boyce
C_{10} = 192571	C_{10} = 180248	μ_1 = 388831	μ = 385143
	C_{01} = 14536	α_1 = 1.827	λ_m = 1445

α_1 and λ_m in Table 3.2 are unitless. The rest of the parameters have the unit of Pascal (Pa). All the models had R^2 = 1, which indicates perfect fitting. Neo-Hookean has less constant compared to other models. Therefore, it was chosen for inverse modeling. For the Neo Hookean model, in the case of uniaxial loading, the following relation exists between engineering stress and stretch ratio:

$$\sigma_{eng} = 2C_{10}(\lambda - \frac{1}{\lambda^2}) \tag{3.1}$$

The stretch ratio is related to engineering strain by the following equation:

$$\lambda = 1 + \varepsilon_{eng} \tag{3.2}$$

After C_{10} parameter was determined from inverse modeling, using the above two equations, the stress strain curve corresponding to the C10 value could be obtained.

3.2 Finite Element Model Updating :

A virtual test was done to determine the number of strain fields required to inversely determine the Neo-Hookean model parameters. In the Abaqus model, Material 1 was defined as having C_{10}=337661 Pa and material 2 was defined as having C_{10}=192571 Pa according to single material uniaxial test results of Specimen 1 (Table 3.3, Page 34). 5N Load was applied. This strain distribution was then used as a target in the inverse modeling process. The results showed that Isight could find C_{10} of the two materials from the strain field corresponding to the maximum load. Therefore during the inverse modeling process, the experimental strain field corresponding to 5N load was set as the target.

3.3 Machine Learning

As a first step of the training data generation process, C_{10} was related to the Youngs modulus. The following relation exists between Young's modulus and shear modulus:

$$G = \frac{E}{2(1+\upsilon)} \tag{3.3}$$

Where G is the shear modulus, υ is Poisson's ratio and E is Young's modulus. C_{10} is related to the shear modulus according to:

$$C_{10} = \frac{G}{2} \tag{3.4}$$

With equation (3.4), together with incompressibility assumption (υ=0.5), equation (3.3) reduces to

$$C_{10} = \frac{E}{6} \tag{3.5}$$

A C10 vs Young's modulus curve was plotted using equation (Figure 3.2, blue line). The range of Young's modulus values plotted is 1.0-2.3 MPa according to experimental observations. A bit of the nearby region indicated in the curve was also considered for training data generation because the linear region of the stress-strain curve can extend up to 40% strain [69]. It is up to the tester to choose the range from which young's modulus will be calculated. In this study young's modulus was calculated using 0-5% true strain but the linear region lasted up to 10% true strain for one of the materials (M2_1, specimen 1). C_{10} also varies with calibration strain. So, considering these facts it's appropriate to include a bit of the surrounding region. Otherwise, the search space would be incomplete. 20000 Pa variation was considered on both sides of the blue line.

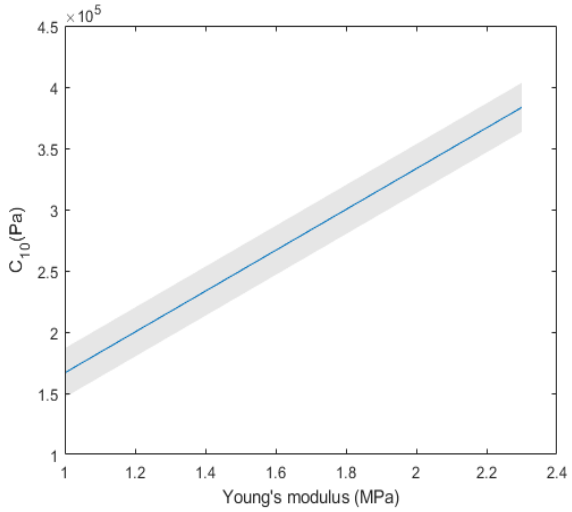

Figure 3.2 Search space for C_{10} for training data generation. Blue line is the plot of Equation (3.5) and shaded region is the uncertainty interval

In the second step, young's modulus combinations (1.0-2.3MPa) in increments of 0.1 MPa- 182 sets and another 118 randomly generated sets, a total of 300 sets were generated. C_{10} corresponding to the young's modulus was assigned to the model and corresponding logarithmic strain of the elements corresponding to 5N load were computed and recorded. The strains were used in the input layer of the DNN and the two C10 parameters (corresponding to M1 and M2) were the targets in

the output layer. 50 synthetic validation data were also generated to evaluate the network performance. The network was trained for 50,000 epochs. The final training loss was .000004. Training time was approximately 10 minutes.

3.4 Results:

All the parameters in this section are reported in Pascal (Pa) unit.

Specimen 1:

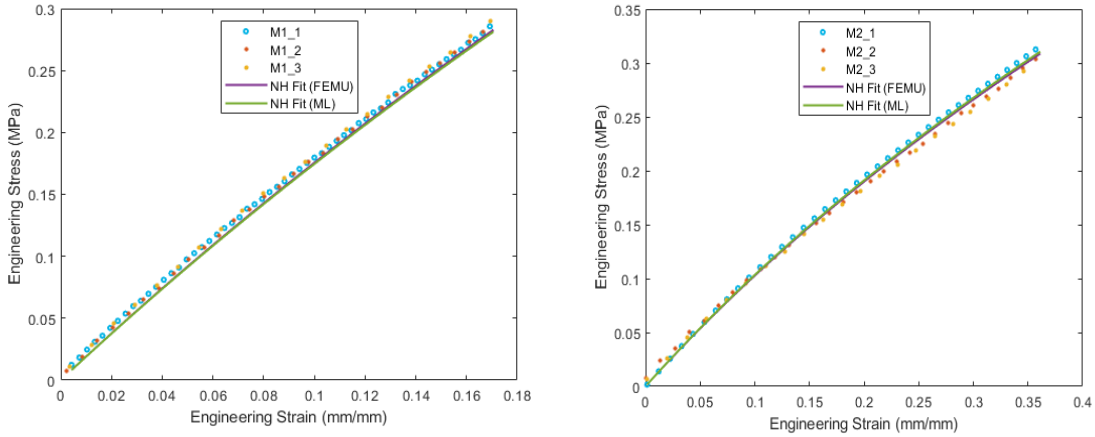

(a) (b)

Figure 3.3 Engineering stress-engineering strain (σ_{eng}-ε_{eng}) plot showing Neo-Hookean fit of (a) M1and (b) M2

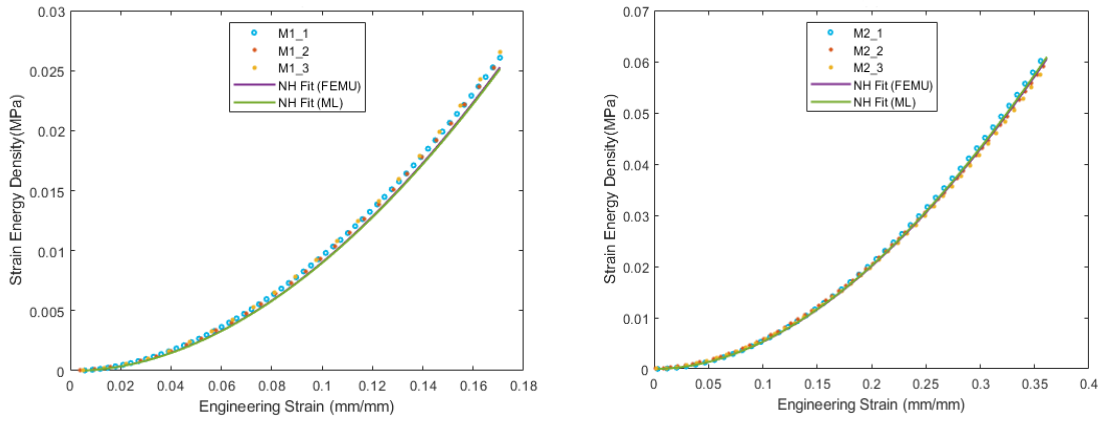

(a) (b)

Figure 3.4 Strain energy density-engineering strain (W-ε_{eng}) plot showing Neo-Hookean fit of (a) M1 and (b) M2

Table 3.3 Single-material uniaxial test results

	Sample 1	Sample 2	Sample 3
C10_M1	337661	335167	342676
C10_M2	192571	190430	187563

Table 3.4 Inverse Modeling Results

	FEMU			ML		
	C_{10}	$R^2(\sigma)$	$R^2(W)$	C_{10}	$R^2(\sigma)$	$R^2(W)$
M1	320744	0.9951	0.9954	319060	0.9937	0.9943
M2	187865	0.9965	0.9991	188950	0.9958	0.999

Specimen 2:

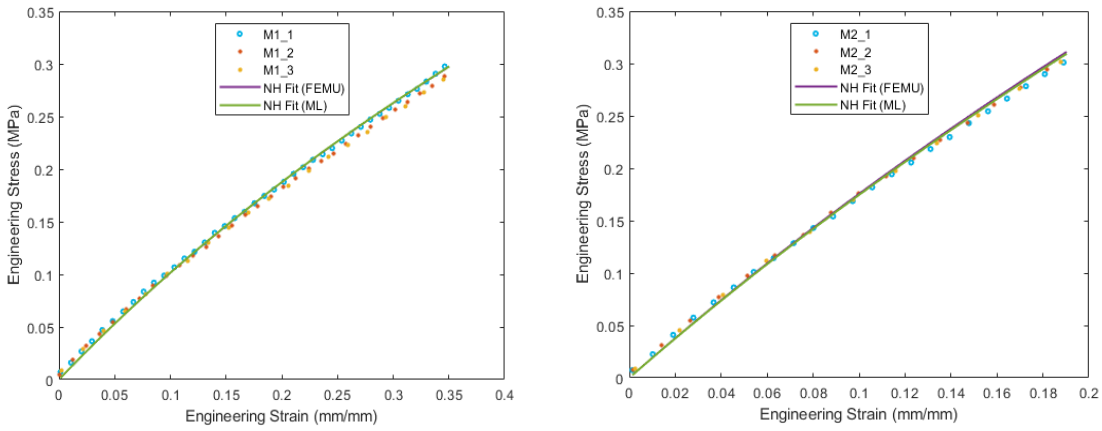

(a) (b)

Figure 3.5 σ_{eng}-ε_{eng} plot showing Neo-Hookean fit of (a) M1and (b) M2

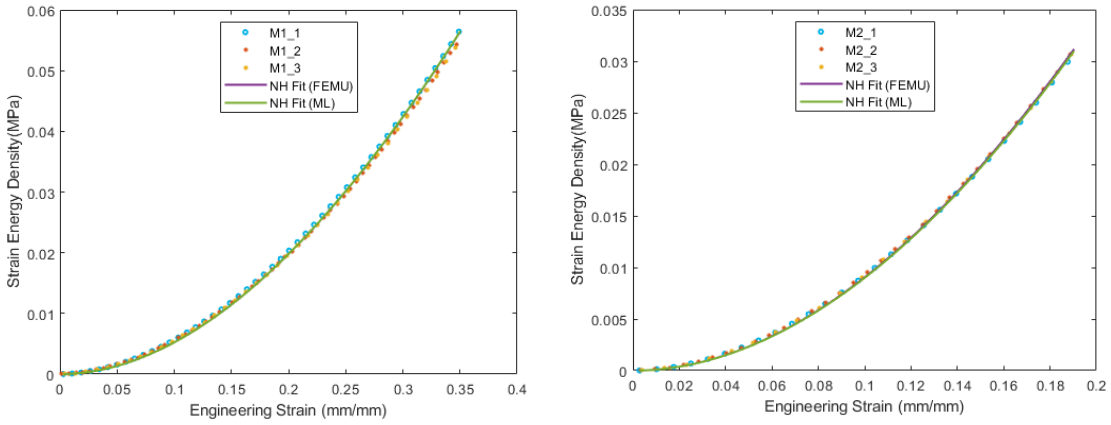

(a) (b)

Figure 3.6 W-ε_{eng} plot showing Neo-Hookean fit of (a) M1 and (b) M2

Table 3.5 Single-material uniaxial test results

i	1	2	3
C_{10}_M1_i	190345	185532	184683
C_{10}_M2_i	324065	327800	326206

Table 3.6 Inverse modeling results

	FEMU			ML		
	C_{10}	$R^2(\sigma)$	$R^2(W)$	C_{10}	$R^2(\sigma)$	$R^2(W)$
M1	185483	0.9955	0.9992	185580	0.9954	0.9991
M2	320970	0.9974	0.9996	319150	0.9981	0.9995

Specimen 3:

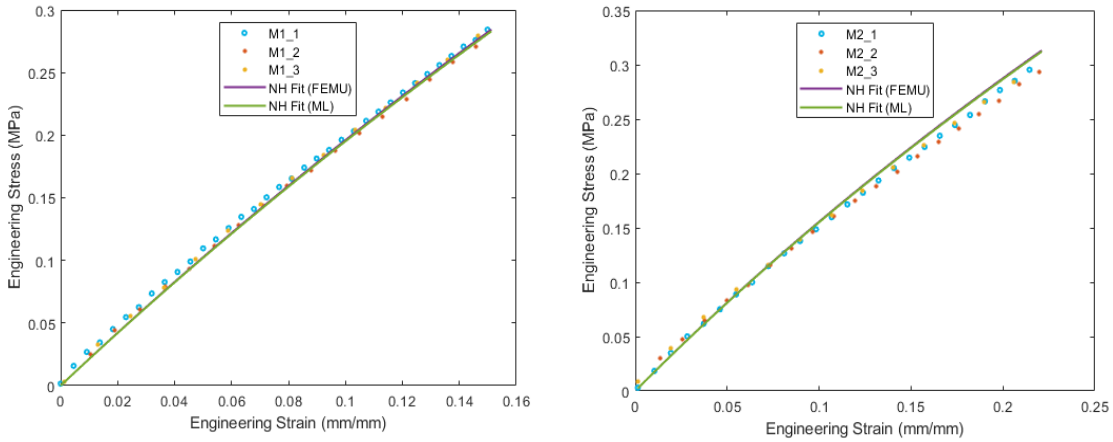

(a) (b)

Figure 3.7 σ_{eng}-ε_{eng} plot showing Neo-Hookean fit of (a) M1 and (b) M2

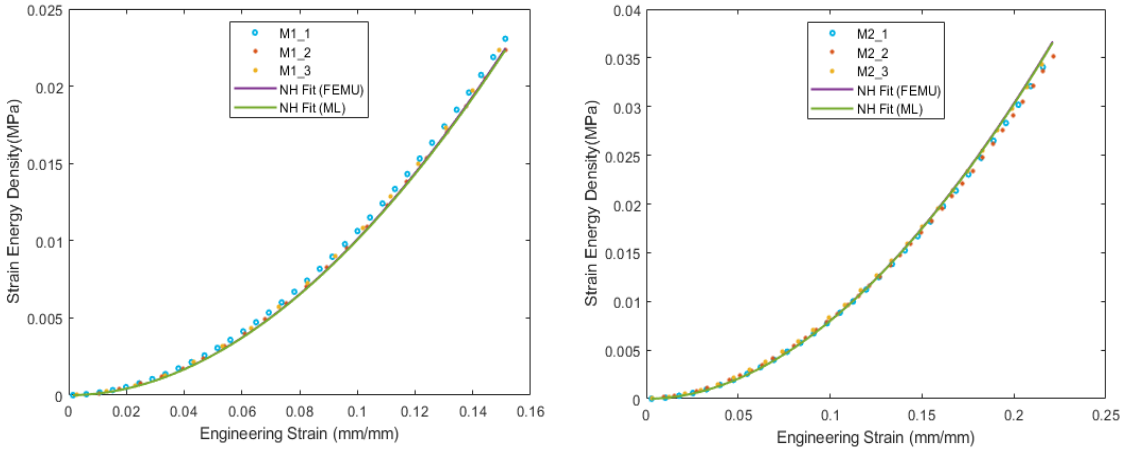

(a) (b)

Figure 3.8 W-ε_{eng} plot showing Neo-Hookean fit of (a) M1 and (b) M2

Table 3.7 Single-material uniaxial test results

i	1	2	3
C_{10}_M1_i	376011	362916	371261
C_{10}_M2_i	280906	280040	287816

Table 3.8 Inverse modeling results

	FEMU			ML		
	C_{10}	$R^2(\sigma)$	$R^2(W)$	C_{10}	$R^2(\sigma)$	$R^2(W)$
M1	358333	0.998	0.9981	356660	0.9976	0.9975
M2	284392	0.9902	0.9983	283600	0.9912	0.9985

Specimen 4:

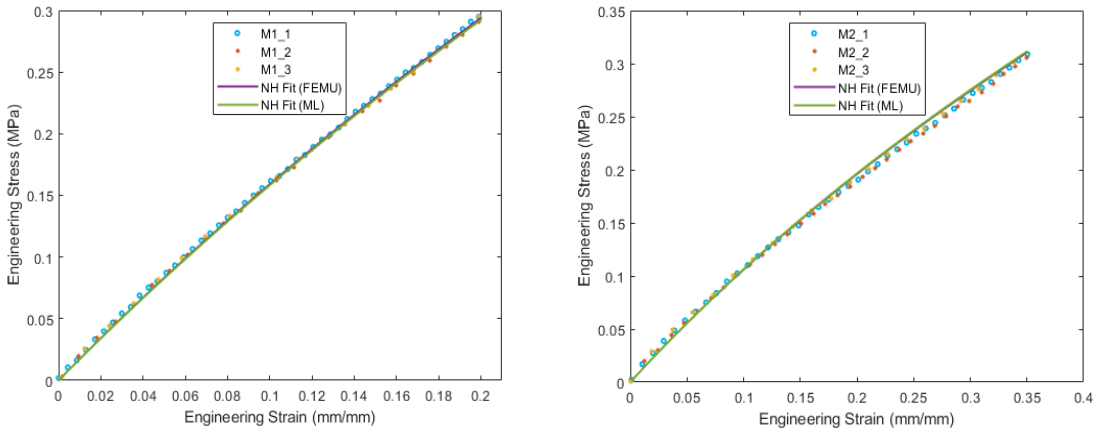

(a) (b)

Figure 3.9 σ_{eng}-ε_{eng} plot showing Neo-Hookean fit of (a) M1and (b) M2

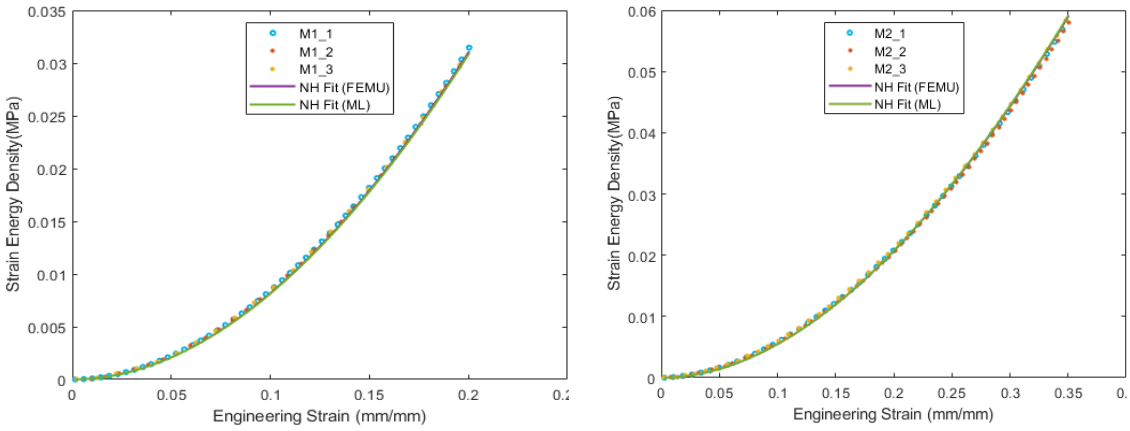

(a) (b)

Figure 3.10 W-ε_{eng} plot showing Neo-Hookean fit of (a) M1 and (b) M2

Table 3.9 Single-material uniaxial test results

i	1	2	3
C_{10}_M1_i	298291	295507	298816
C_{10}_M2_i	195786	193564	198393

Table 3.10 Inverse modeling results

	FEMU			ML		
	C_{10}	$R^2(\sigma)$	$R^2(W)$	C_{10}	$R^2(\sigma)$	$R^2(W)$
M1	290580	0.9992	0.9995	289050	0.9991	0.9992
M2	193853	0.9969	0.9994	194340	0.9965	0.9993

Specimen 5:

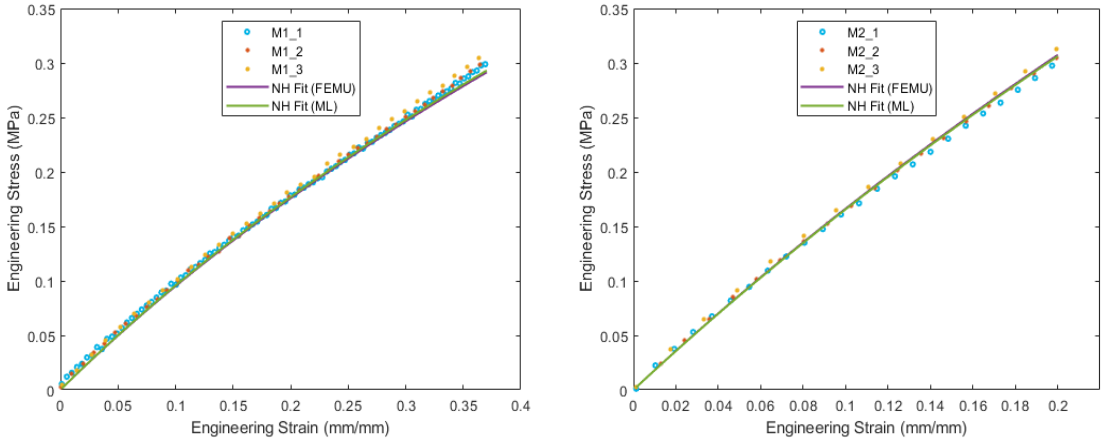

(a) (b)

Figure 3.11 σ_{eng}-ε_{eng} plot showing Neo-Hookean fit of (a) M1and (b) M2

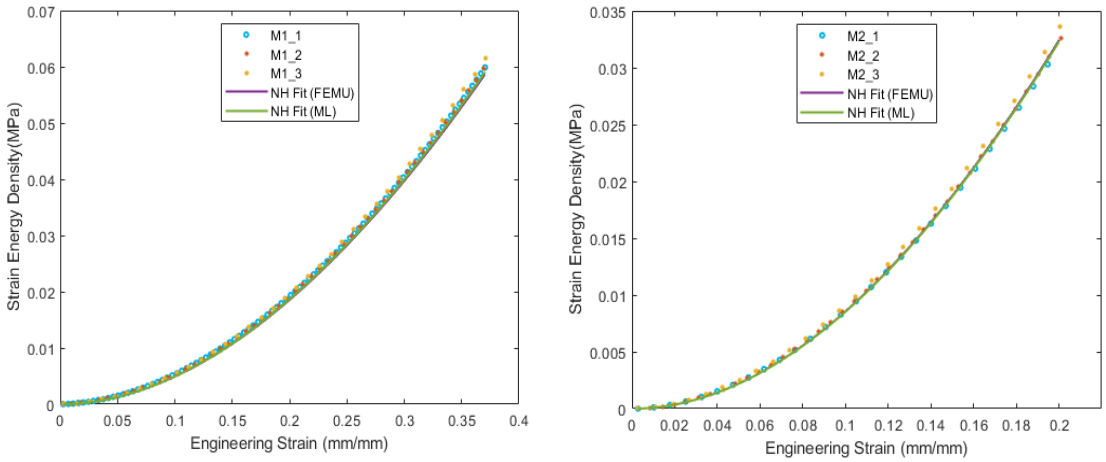

(a) (b)

Figure 3.12 W-ε_{eng} plot showing Neo-Hookean fit of (a) M1 and (b) M2

Table 3.11 Single-material uniaxial test results

i	1	2	3
C_{10}_M1_i	180521	180620	185155
C_{10}_M2_i	297562	306757	319445

Table 3.12 Inverse modeling results

	FEMU			ML		
	C_{10}	$R^2(\sigma)$	$R^2(W)$	C_{10}	$R^2(\sigma)$	$R^2(W)$
M1	173928	0.995	0.9972	174880	0.9962	0.9979
M2	303848	0.9976	0.9986	302760	0.9976	0.9984

3.5 Discussion:

Inverse modeling was done using two strain fields (corresponding to 2.5N and 5N) and three strain fields (corresponding to 1N, 2.5N, and 5N) to see if the increasing number of strain fields improved the results. However, no significant improvement was observed.

A R^2 value greater than 0.90 is termed good by many researchers [60,62,73,74]. For direct problem where experimental stress-strain is available, R^2 values very close to 1 is often obtained. However, when the problem is complex, this is not the case. The direct problem can also be difficult sometimes. R. W. Ogden termed experimental data fitting within the mechanics or thermo-mechanics framework of elastomeric solids as ‘a very delicate question’ [75]. In the study conducted by Tobajas et al [60], the best fit obtained had a corresponding R^2 value of 0.9783. In another study. For most of the materials in this study in moderate strain range, the R^2 value was greater than 0.996. Since this is an inverse problem, this is a good accuracy.

Table 3.13 shows the time taken by the two methods. Machine learning method is significantly faster.

Table 3.13 Comparison of time taken by the two methods

Method	FEMU	ML
Time (sec)	~5400	<.001

CHAPTER IV

INVERSE MODELING IN LARGE STRAIN RANGE

4.1 Model Selection:

We define high strain as the strain level when the stress-strain curve has the typical S shape of hyperelastic materials. As described in section 2.2.2, for large strain range, 18N was the maximum load considered. Table 4.1 shows calibration strain (%) obtained from full field strain distribution corresponding to 18N load.

Table 4.1 Calibration strain (%) obtained from full field strain distribution corresponding to 18N load

Specimen 1		Specimen 2		Specimen 3		Specimen 4		Specimen 5	
M1	M2	M1	M2	M1	M2	M1	M2	M1	M2
53	90	88	56	50	63	59	87	93	58

Based on literature review, Ogden and Yeoh models fit well in this region. Figure 4.1 shows how the models fit the experimental data of one of the materials (Specimen 1, M2_1) in this study.

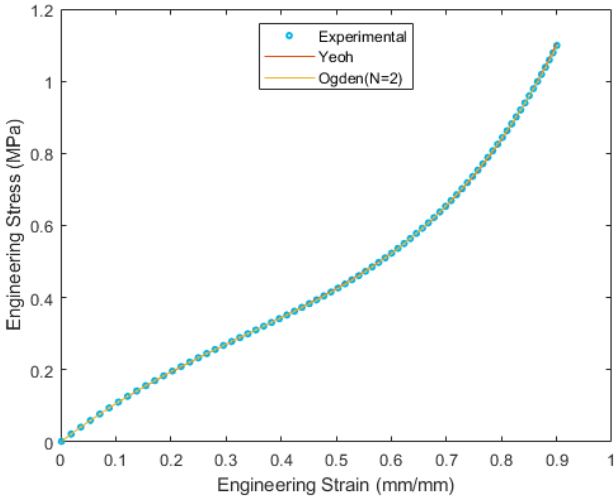

Figure 4.1 Ogden and Yeoh Model Fit to experimental data

Table 4.2 Yeoh and Ogden model parameters

Yeoh		Ogden (N=2)	
C_{10}	194494	μ_1	10200
C_{20}	-15066	μ_2	380000
C_{30}	23377	α_1	9.92
		α_2	0.987

Both models can fit experimental data perfectly. Yeoh model has one less parameter than the Ogden model. This is convenient for the inverse modeling process. More than one deformation mode is suggested to properly characterize the material when using the Ogden model [54]. Parameters determined with only uniaxial test may not represent other deformation modes well. Keerthiwansa et al [76] compared hyperelastic model parameters determined from only uniaxial data and a combination of uniaxial and pure shear data. For the Mooney-Rivlin model combination of two test data significantly improved the quality of fit while the Yeoh model was found to be less responsive to the change. Therefore, Yeoh model was chosen in this study for high strain characterization. For

Yeoh model, in case of uniaxial loading, the following relation exists between engineering stress and stretch ratio:

$$\sigma_{eng} = \sum_{i=1}^{3} 2i\left(\lambda - \frac{1}{\lambda^2}\right) C_{i0}(I_1 - 3)^{i-1} \tag{4.1}$$

Where, $I_1 = \lambda^2 + \frac{2}{\lambda}$

4.2 Finite Element Model Updating

Now we closely examine the three parameters of the Yeoh model. Figure 4.2 shows how C_{10}, C_{20}, and C_{30} influence the stress-strain curve. Typically, C_{10} is positive, C_{20} is negative and C30 is positive. These magnitudes create the typical S shape. At low strains, C_{10} represents the initial shear modulus, which softens because of the influence of negative C_{20}, and an upturn follows because of positive C_{30} at larger strains. Therefore, the initial assumption was that at least three strain fields corresponding to three regions will be needed to inversely determine the three parameters.

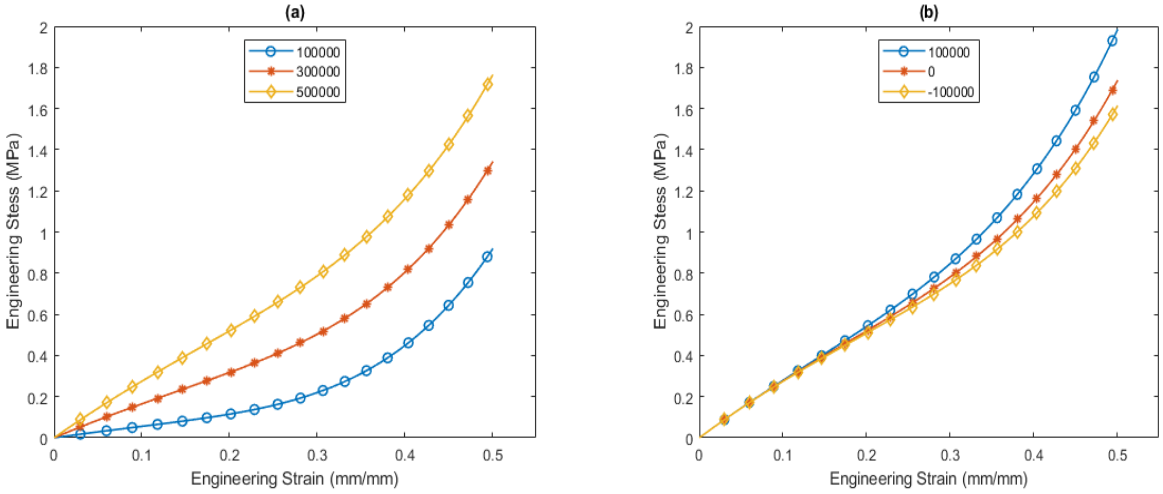

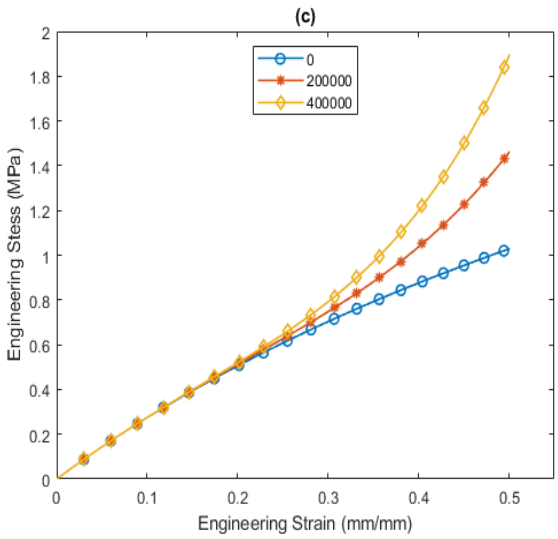

Figure 4.2 Influence of the three parameters on the stress-strain curve (a) shows stress-strain curves with fixed values of C_{20}, C_{30}, and varying C_{10}. Figure (b) shows stress-strain curves with fixed values of C_{10}, C_{30}, and varying C_{20}. Figure (c) shows stress-strain curves with fixed values of C_{10}, C_{20}, and varying C_{30}

Figure 4.3 shows virtual test results where material 1 had C_{10}= 334466, C_{20}= -17853, C_{30}=124079 and material 2 had C_{10}= 193655, C_{20}= -15219, C_{30}=22227 according to Specimen 1 test results (Table 4.3, Page 50). One strain field (corresponding to 18N) is not enough to inversely determine the three parameters. Inverse modeling results were identical to target values with three strain fields (corresponding to 2N,10N, and 18N).

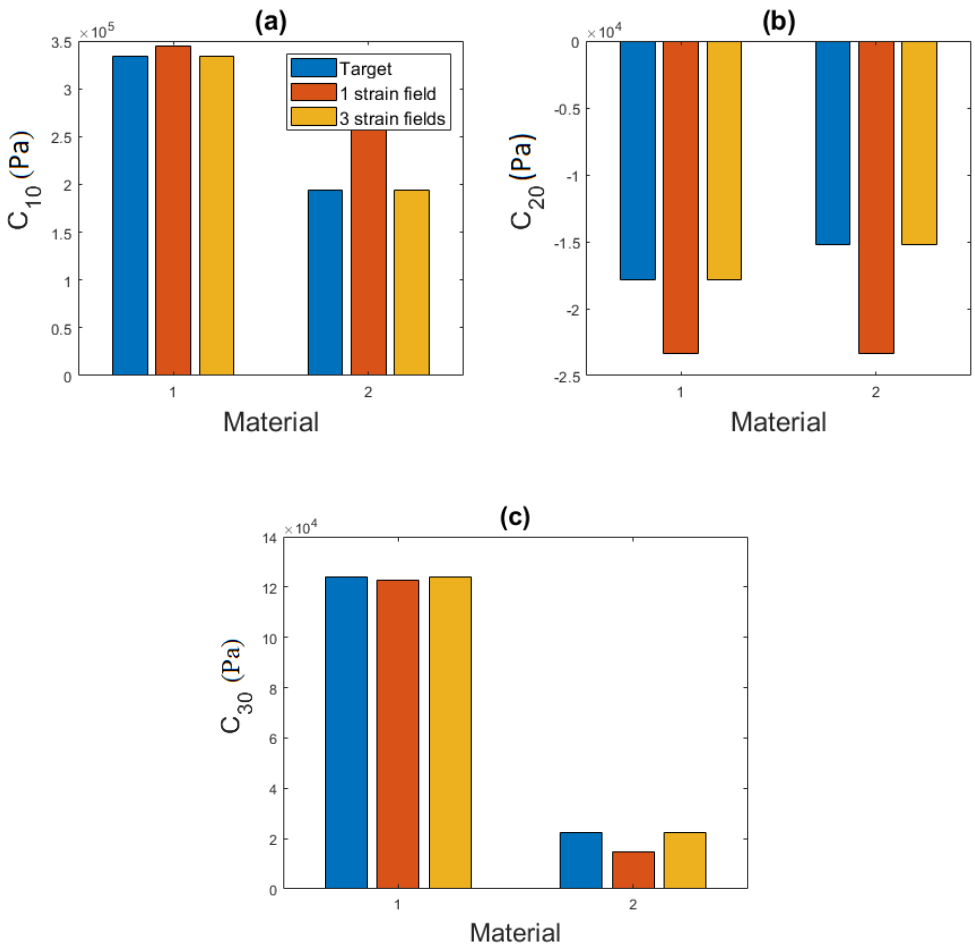

Figure 4.3 Virtual test results

4.3 Machine Learning:

Figure 4.4 (a) shows the stress-strain curve of specimen 5, M1_1 up to 75% engineering strain. Figure 4.4 (b),(c), and (d) show how the three parameters (C_{10}, C_{20}, and C_{30}) vary with calibration strain. A 30 % calibration strain, for example, in the plots means that the Yeoh model parameters were obtained through curve fitting of 0-30% engineering stress-engineering strain curve. C_{10} is the most stable parameter among the three. C_{20} starts at a high negative value which gradually increases with an increase in calibration strain. C_{30} value gradually decreases and almost stabilizes when the stress-strain curve has the S shape or in other words when the upturn has begun. For material with higher Young's modulus, C_{30} stabilizes at a higher value.

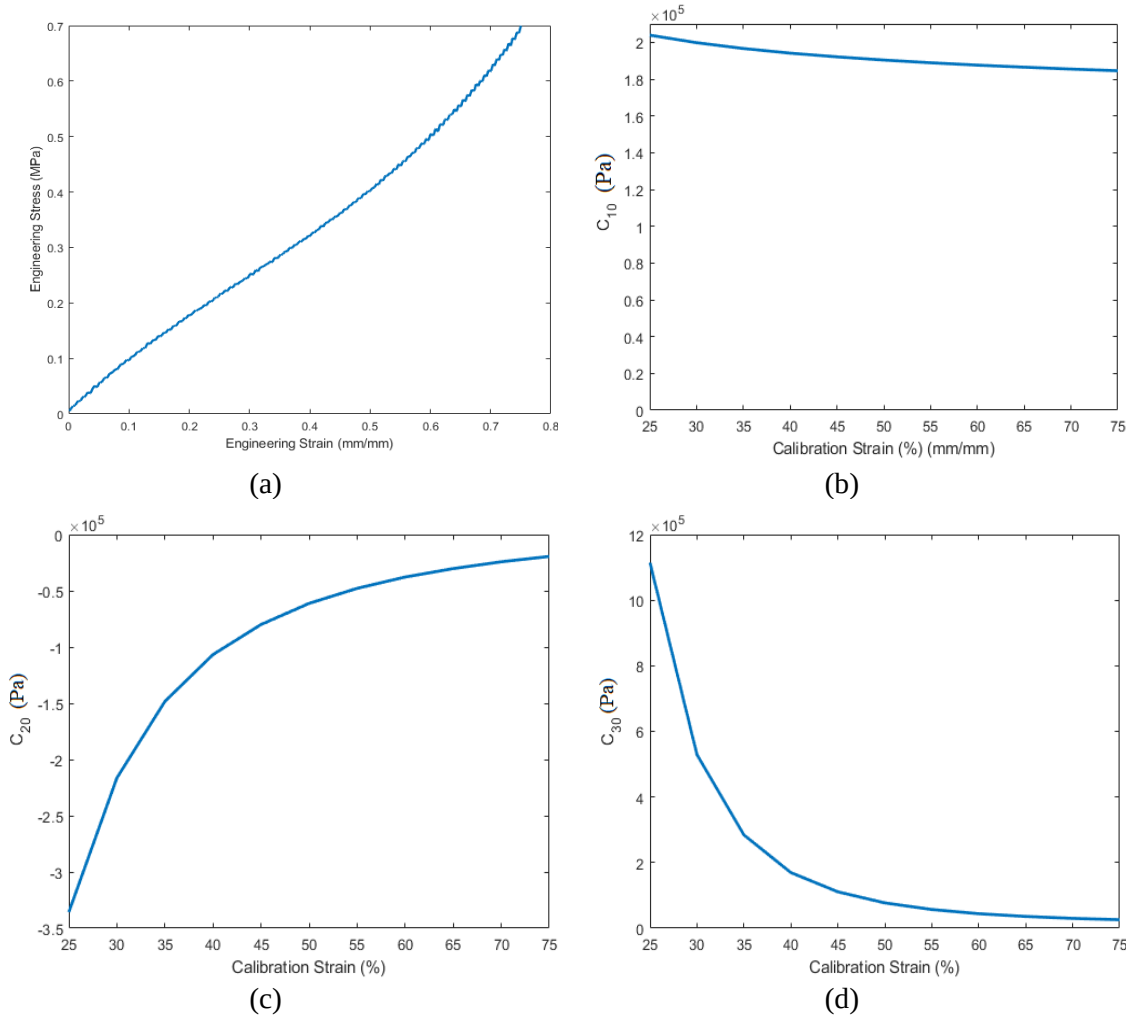

Figure 4.4 (a) Stress-strain curve of M1_1 of Specimen 5 (b) Variation of C_{10} with calibration strain (c) Variation of C_{20} with calibration strain (d) Variation of C_{30} with calibration strain

For materials with different Young's modulus, C_{30} values were obtained when the stress-strain curve corresponding to the materials had an S shape. Then the values were plotted against Young's modulus and the blue line in Figure 4.5 was obtained. A few surrounding values were also considered since the C_{30} values didn't fully stabilize. A 3000Pa variation was considered for C_{30} value corresponding to 1.1 Mpa Young's modulus and 30000Pa variation was considered for C_{30} value corresponding to 2.3 Mpa. The variation varied linearly in between.

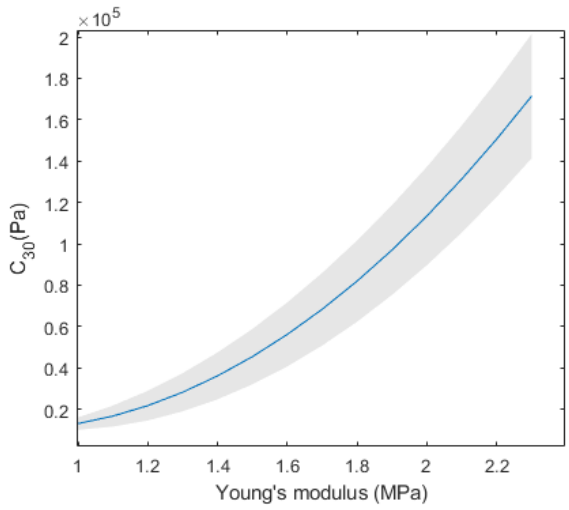

Figure 4.5 C30 vs Young's modulus

For generating training data, the following equation was obtained through curve fitting:

$$C_{30} = (7.1227 \times 10^4)\mathrm{YM}^2 + (-1.1328 \times 10^5)\mathrm{YM} + (5.5097 \times 10^4) \quad (4.2)$$

Here, YM is Young's modulus. Young's modulus combinations were generated in the same way as in the case of inverse modeling in moderate strain range. Since in this case there are two additional parameters, more random combinations (304) were used during training so that the entire search space is covered. In total 500 combinations were used for training data generation. Then the C_{10} and C_{30} corresponding to the young's modulus were assigned to the model and the corresponding logarithmic strain of the elements corresponding to 2N, 10N, and 18N load were computed and recorded. The C_{20} parameter was kept random (a value between -40000Pa and -5000Pa according to experimental observation). The strains were used in the input layer of the DNN and the six parameters (two C_{10}, two C_{20}, and two C_{30} corresponding to M1 and M2) were the targets in the output layer. 100 synthetic validation data were also generated to evaluate the network performance. The network was trained for 120,000 epochs. The final training loss was .06. Training time was approximately 30 minutes.

4.4 Results:

All the parameters in this section are reported in Pascal (Pa) unit.

Specimen 1:

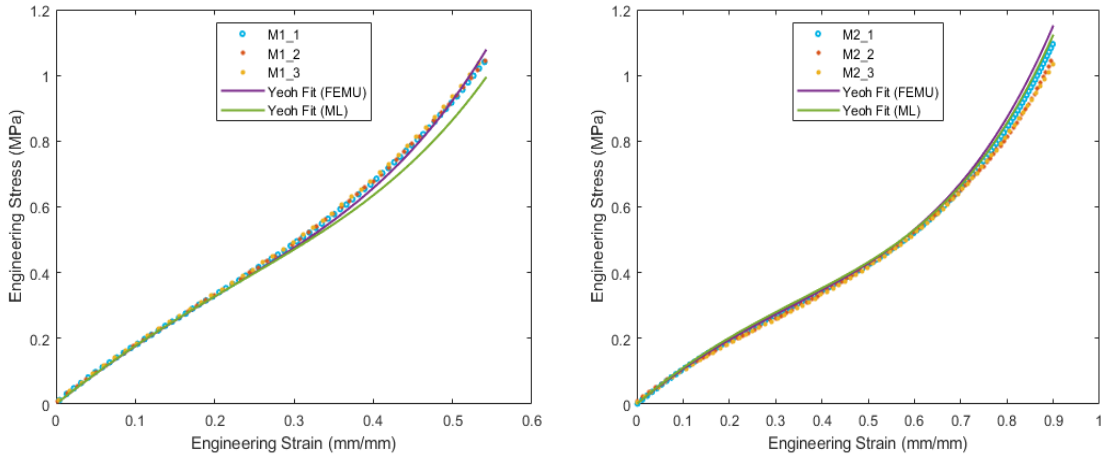

(a) (b)

Figure 4.6 σ_{eng}-ε_{eng} plot showing Yeoh fit of (a) M1and (b) M2

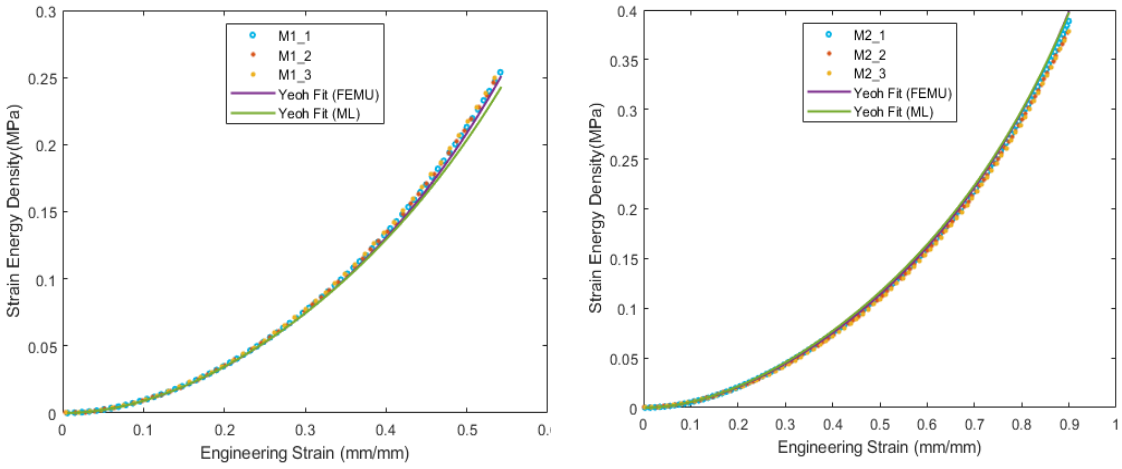

(a) (b)

Figure 4.7 W-ε_{eng} plot showing Yeoh fit of (a) M1 and (b) M2

Table 4.3 Single-material uniaxial test results

i	1	2	3	j	1	2	3
C_{10}_M1_i	334466	337763	342957	C_{10}_M2_j	193655	194494	190247
C_{20}_M1_i	-17853	-32187	-36154	C_{20}_M2_j	-15219	-15067	-14126
C_{30}_M2_i	124079	135684	142420	C_{30}_M2_j	22227	23378	22205

Table 4.4 Inverse modeling results

	FEMU		ML	
	M1	M2	M1	M2
C_{10}	322082	196063	324610	203040
C_{20}	-15231	-16825	-20740	-21270
C_{30}	130626	25862	106990	25760
$R^2(\sigma)$	0.9974	0.987	0.9843	0.9928
$R^2(W)$	0.998	0.9972	0.9928	0.9963

Specimen 2:

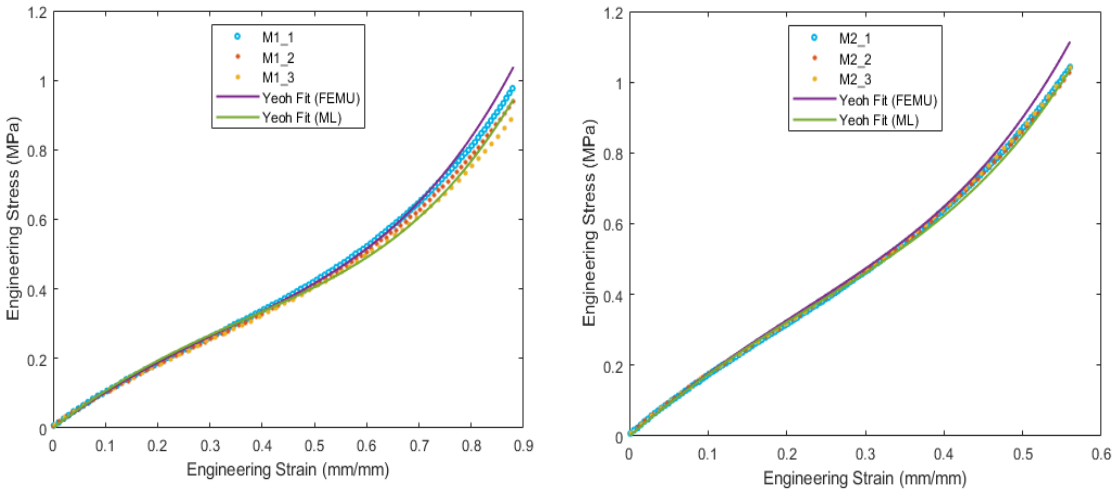

(a) (b)

Figure 4.8 σ_{eng}-ε_{eng} plot showing Yeoh fit of (a) M1and (b) M2

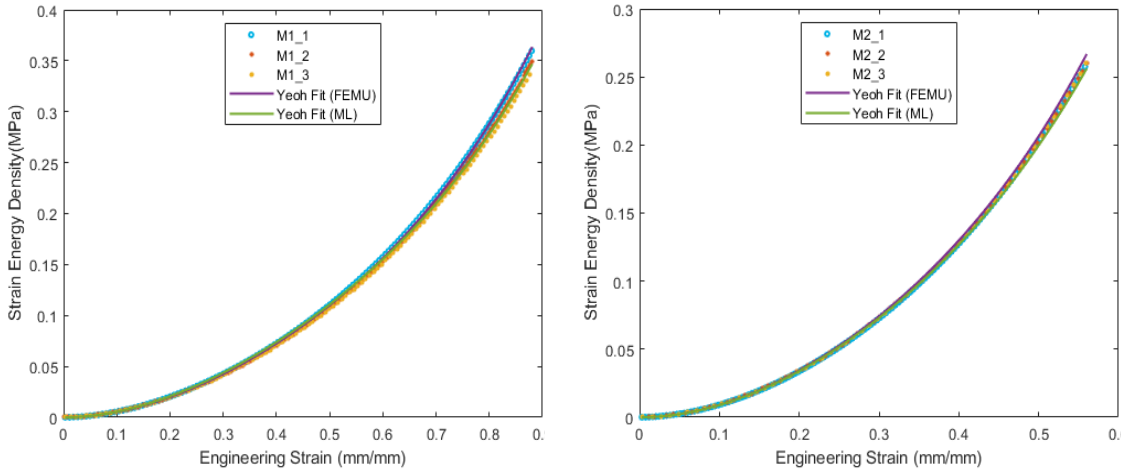

(a) (b)

Figure 4.9 W-ε_{eng} plot showing Yeoh fit of (a) M1 and (b) M2

Table 4.5 Single-material uniaxial test results

i	1	2	3	j	1	2	3
C_{10}_M1_i	192722	187885	187522	C_{10}_M2_j	325057	329296	327166
C_{20}_M1_i	-12991	-12672	-14020	C_{20}_M2_j	-33953	-39197	-31768
C_{30}_M2_i	20932	19819	186641	C_{30}_M2_j	121072	120233	117502

Table 4.6: Inverse Modeling Results

	FEMU		ML	
	M1	M2	M1	M2
C_{10}	187579	322966	195730	319210
C_{20}	-11662	-17566	-23210	-23090
C_{30}	22721	121440	22710	107240
$R^2(\sigma)$	0.982	0.9938	0.9942	0.9982
$R^2(W)$	0.9974	0.9991	0.9986	0.9995

Specimen 3:

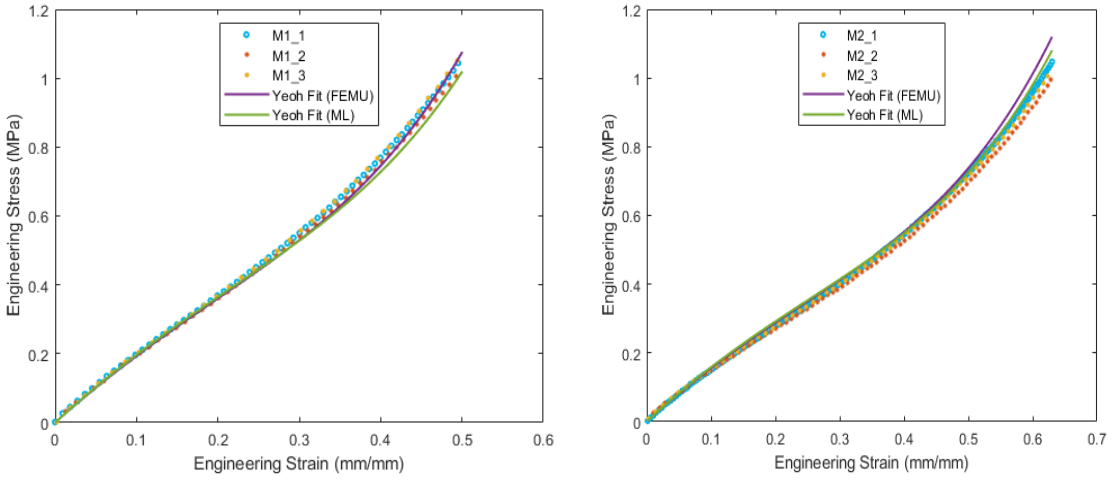

(a) (b)

Figure 4.10 σ_{eng}-ε_{eng} plot showing Yeoh fit of (a) M1and (b) M2

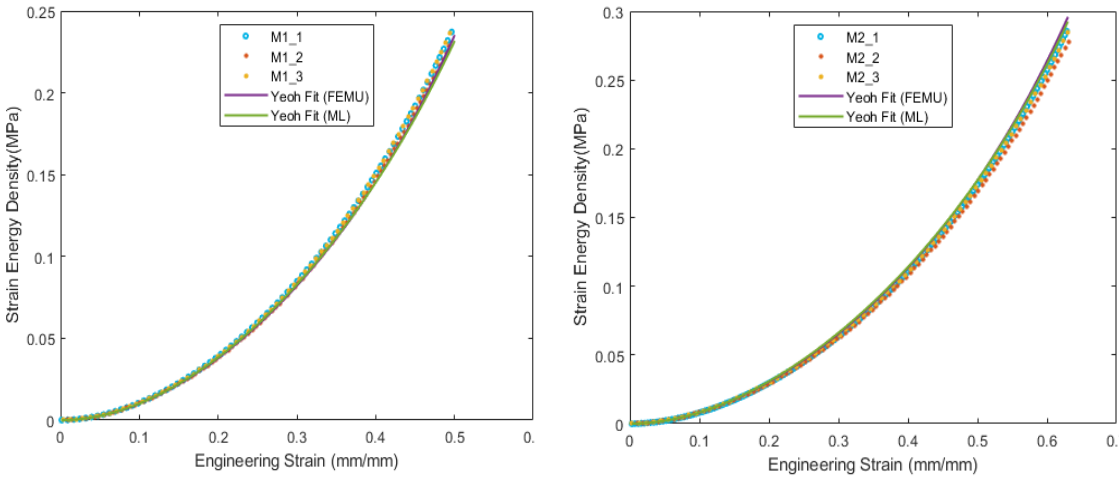

(a) (b)

Figure 4.11 W-ε_{eng} plot showing Yeoh fit of (a) M1 and (b) M2

Table 4.7 Single-material uniaxial test results

i	1	2	3	j	1	2	3
C_{10}_M1_i	375005	361744	369783	C10_M2_j	280686	282671	289684
C_{20}_M1_i	-39537	-21425	-18591	C20_M2_j	-8966	-34096	-31552
C_{30}_M2_i	181327	159927	168124	C30_M2_j	66990	78478	77275

Table 4.8 Inverse Modeling Results

	FEMU		ML	
	M1	M2	M1	M2
C_{10}	353961	285546	359420	290290
C_{20}	-14786	-15431	-19190	-21500
C_{30}	168922	80251	142420	76110
R2(σ)	0.9972	0.9853	0.992	0.9937
R2(W)	0.9982	0.9962	0.9975	0.9969

Specimen 4:

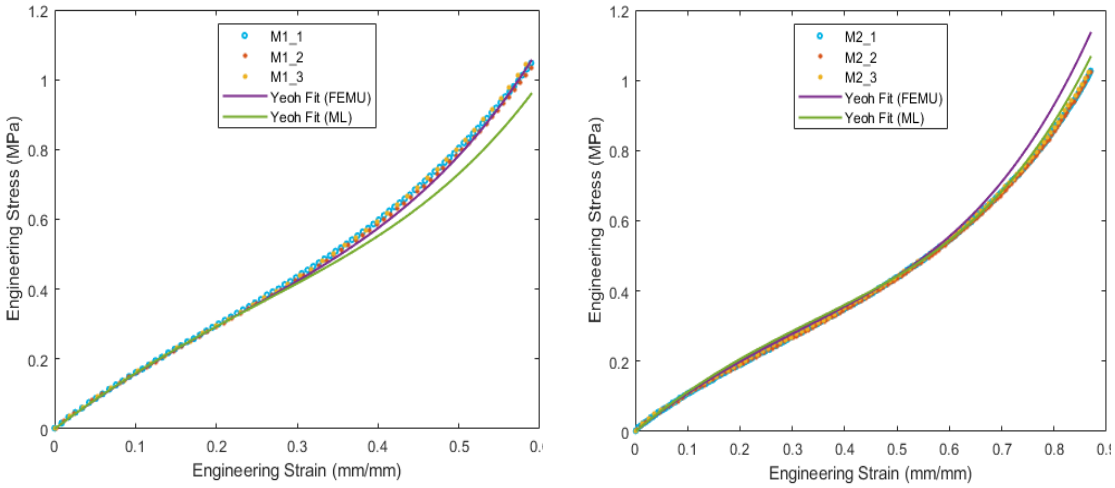

(a) (b)

Figure 4.12 σ_{eng}-ε_{eng} plot showing Yeoh fit of (a) M1and (b) M2

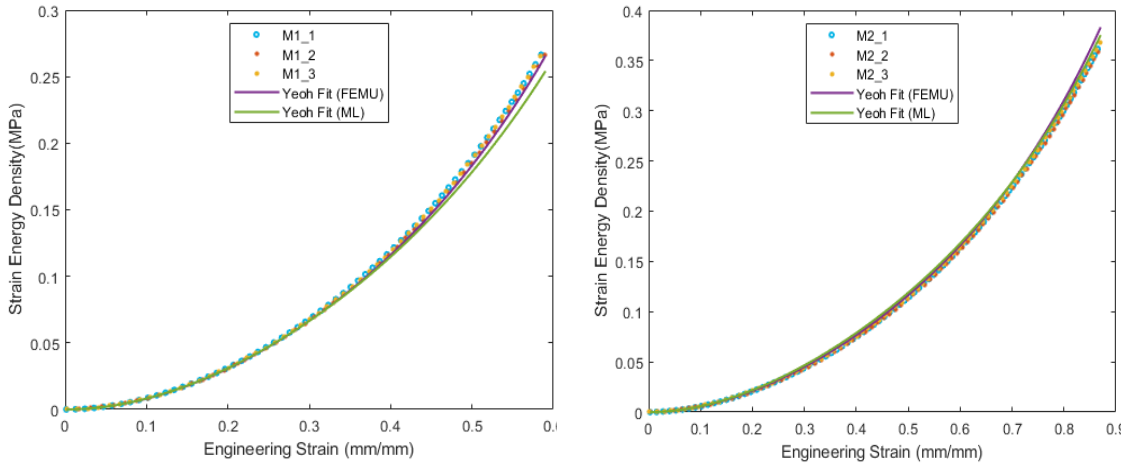

(a) (b)

Figure 4.13 W-ε_{eng} plot showing Yeoh fit of (a) M1 and (b) M2

Table 4.9 Single-material uniaxial test results

i	1	2	3	j	1	2	3
C_{10}_M1_i	297754	295584	298817	C_{10}_M2_j	198425	196130	202116
C_{20}_M1_i	-5308	-13854	-16422	C_{20}_M2_j	-13991	-13774	-18179
C_{30}_M2_i	84847	90198	98218	C_{30}_M2_j	23577	23655	25469

Table 4.10 Inverse Modeling Results

	FEMU		ML	
	M1	M2	M1	M2
C_{10}	287615	198953	291410	207270
C_{20}	-6027	-15259	-20550	-21550
C_{30}	88495	28159	77210	26770
$R^2(\sigma)$	0.998	0.9814	0.9752	0.9971
$R^2(W)$	0.9988	0.9974	0.9936	0.9982

Specimen 5:

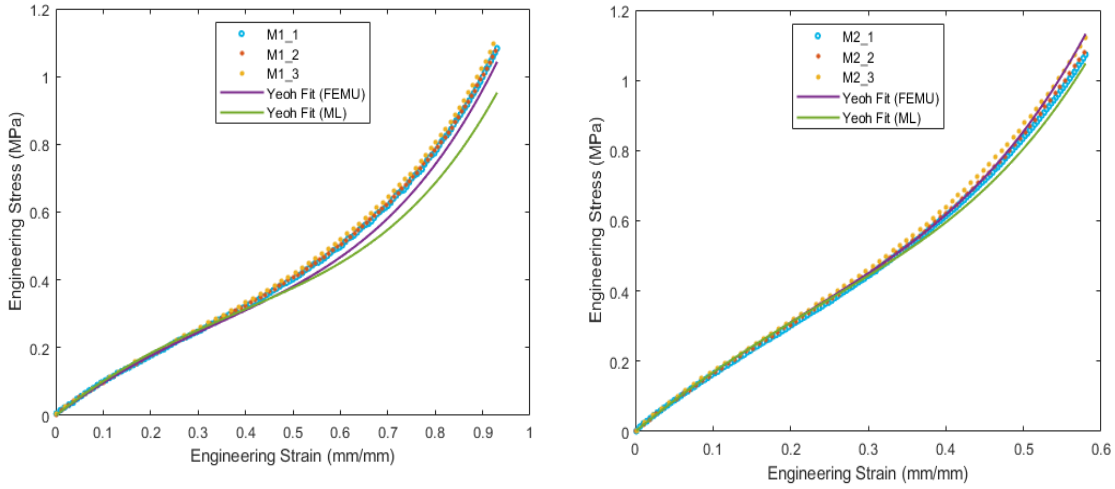

(a) (b)

Figure 4.14 σ_{eng}-ε_{eng} plot showing Yeoh fit of (a) M1and (b) M2

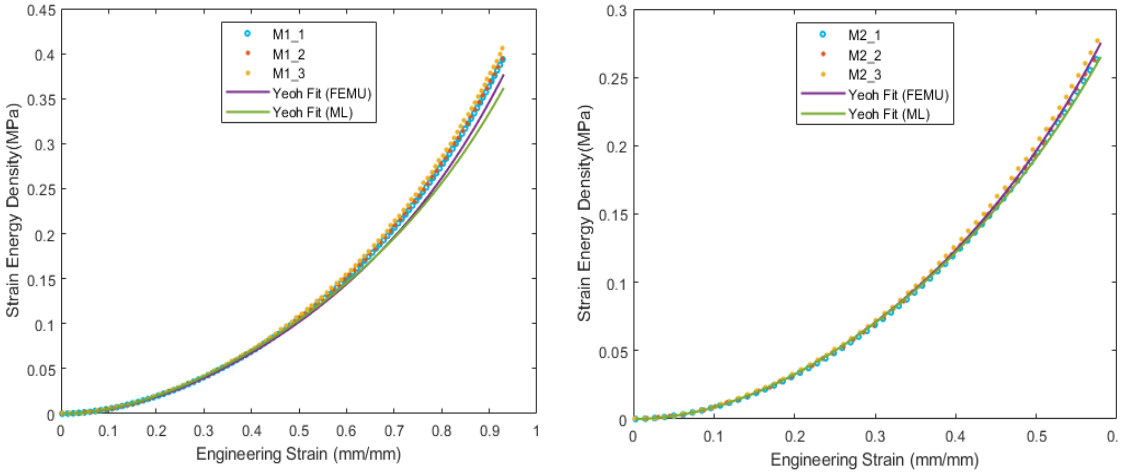

(a) (b)

Figure 4.15 W-ε_{eng} plot showing Yeoh fit of (a) M1 and (b) M2

Table 4.11 Single-material uniaxial test results

i	1	2	3	j	1	2	3
C_{10}_M1_i	182475	181904	186364	C10_M2_j	303667	306309	31998
C_{20}_M1_i	-10659	-8080	-75590	C20_M2_j	-10370	-7791	-22350
C_{30}_M2_i	19706	18808	18991	C30_M2_j	99560	99090	113696

Table 4.12 Inverse Modeling Results

	FEMU		ML	
	M1	M2	M1	M2
C_{10}	175805	305942	185970	308250
C_{20}	-13616	-11046	-24050	-23150
C_{30}	19957	109430	19890	98250
$R^2(\sigma)$	0.9851	0.9977	0.9421	0.99
$R^2(W)$	0.9903	0.9992	0.9824	0.9972

4.5 Discussion

Inverse modeling was done using five strain fields (corresponding to 2N, 6N, 10N, 14N, and 18N) to see if the increasing number of strain fields improved the results. However, no significant improvement was observed. Therefore, future studies will utilize three strain fields that correspond to low, moderate, and high strain levels for inverse modeling.

Accuracy was slightly lower in large strain range compared to moderate strain range. One of the possible reasons is inaccuracy associated with high strain DIC [77]. For high strain DIC, only one reference image is not sufficient. A few images have to be given as input for the analysis. The reference image is updated based on an algorithm in the software. Figure 4.16 shows a section of a speckle pattern corresponding to two loads.

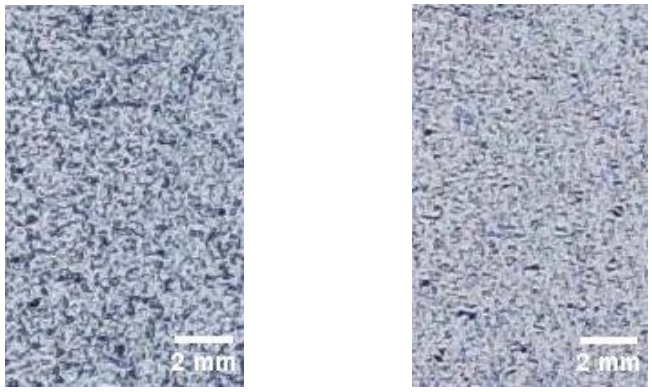

(a) (b)

Figure 4.16 A section of the speckle pattern at various loads (a) 0N (b) 10N

Table 4.13 Mean Intensity Gradient of the speckle pattern corresponding to various loads

Load (N)	0	10
MIG	28.022	21.1650

At higher loads mean intensity gradient value is lower. So, if this image is used as a reference image at some point during the analysis, it will yield some inaccuracy.

Table 4.14 shows the time taken by the two methods. The machine learning method is significantly faster.

Table 4.14 Comparison of time taken by the two methods

Method	FEMU	ML
Time(sec)	~14400	<.001

CHAPTER V

CONCLUSIONS AND FUTURE WORK

5.1 Conclusions:

a) Both the inverse methods, traditional FEMU and the developed ML method in this work, are capable of inversely solving hyperelastic material parameters for the demonstrated case studies with simple flat, 1×2 heterogeneous patterns, in both the moderate and large strain ranges, and their accuracy is comparable.

b) Higher accuracy is obtained in the moderate strain range inverse modeling compared to that of the high strain range.

c) The machine Learning method has a significant advantage in efficiency compared to FEMU – more than six orders of magnitude faster in the demonstrated case studies.

5.2 Future Work:

a) Future work will aim at solving more complex patterns. The immediate next step will be to solve the 2×2 grid pattern consisting of four different materials.

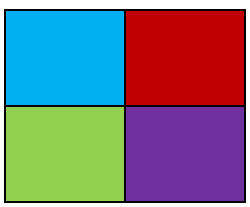

Figure 5.1 2×2 grid pattern

b) In this study, hyperelastic model parameters were determined using a uniaxial test only. For complete characterization, more deformation modes are needed since in actual applications the materials can undergo more than one deformation mode. Characterization by the method in this study is not complete. But it can be considered as a good approximation. In future studies, more deformation modes will be tested.

REFERENCES

[1] Wang, B., Ghanta, P., Vinnikova, S., Bao, S., Liang, J., Lu, H., and Wang, S., 2017, "Wrinkling of Tympanic Membrane under Unbalanced Pressure," J. Appl. Mech., **84**(4), p. 041002.

[2] Rensink, M. J., 2012, "Through the Otoscope: Symptoms Poor Hearing and Wrinkled Tissue," Hear. J., **65**(7), pp. 8–10.

[3] Jett, S., Laurence, D., Kunkel, R., Babu, A. R., Kramer, K., Baumwart, R., Towner, R., Wu, Y., and Lee, C.-H., 2018, "An Investigation of the Anisotropic Mechanical Properties and Anatomical Structure of Porcine Atrioventricular Heart Valves," J. Mech. Behav. Biomed. Mater., **87**, pp. 155–171.

[4] Greve, M. W., and Zink, B. J., 2009, "Pathophysiology of Traumatic Brain Injury," Mt. Sinai J. Med. J. Transl. Pers. Med. J. Transl. Pers. Med., **76**(2), pp. 97–104.

[5] Dehoff, P. H., 1978, "On the Nonlinear Viscoelastic Behavior of Soft Biological Tissues," J. Biomech., **11**(1–2), pp. 35–40.

[6] Rogers, J. A., Someya, T., and Huang, Y., 2010, "Materials and Mechanics for Stretchable Electronics," science, **327**(5973), pp. 1603–1607.

[7] Körner, C., and Singer, R. F., 2000, "Processing of Metal Foams—Challenges and Opportunities," Adv. Eng. Mater., **2**(4), pp. 159–165.

[8] Feng, J., 2017, "Preparation and Properties of Poly (Lactic Acid) Fiber Melt Blown Non-Woven Disordered Mats," Mater. Lett., **189**, pp. 180–183.

[9] Suo, Z., 2012, "Mechanics of Stretchable Electronics and Soft Machines," Mrs Bull., **37**(3), pp. 218–225.

[10] Gray, H., 1924, *Anatomy of the Human Body*, Lea & Febiger.

[11] Wu, X., and Zhu, Y., 2017, "Heterogeneous Materials: A New Class of Materials with Unprecedented Mechanical Properties," Mater. Res. Lett., **5**(8), pp. 527–532.

[12] Smith, K. C. A., and Oatley, C. W., 1955, "The Scanning Electron Microscope and Its Fields of Application," Br. J. Appl. Phys., **6**(11), p. 391

[13] Jalili, N., and Laxminarayana, K., 2004, “A Review of Atomic Force Microscopy Imaging Systems: Application to Molecular Metrology and Biological Sciences,” Mechatronics, **14**(8), pp. 907–945.

[14] Binnig, G., and Rohrer, H., 2000, “Scanning Tunneling Microscopy,” IBM J. Res. Dev., **44**(1/2), p. 279.

[15] Surman, S. B., Walker, J. T., Goddard, D. T., Morton, L. H. G., Keevil, C. W., Weaver, W., Skinner, A., Hanson, K., Caldwell, D., and Kurtz, J., 1996, “Comparison of Microscope Techniques for the Examination of Biofilms,” J. Microbiol. Methods, **25**(1), pp. 57–70.

[16] Li, S., Xu, Z., Reading, I., Yoon, S. F., Fang, Z. P., and Zhao, J., 2008, “Three Dimensional Sidewall Measurements by Laser Fluorescent Confocal Microscopy,” Opt. Express, **16**(6), pp. 4001–4014.

[17] Gräf, R., Rietdorf, J., and Zimmermann, T., 2005, “Live Cell Spinning Disk Microscopy,” Microsc. Tech., pp. 57–75.

[18] Boyde, A., 1989, “Combining Confocal and Conventional Modes in Tandem Scanning Reflected Light Microscopy,” Scanning, **11**(3), pp. 147–152.

[19] Chu, T. C., Ranson, W. F., and Sutton, M. A., 1985, “Applications of Digital-Image-Correlation Techniques to Experimental Mechanics,” Exp. Mech., **25**(3), pp. 232–244.

[20] Peters, W. H., Ranson, W. F., Sutton, M. A., Chu, T. C., and Anderson, J., 1983, “Application of Digital Correlation Methods to Rigid Body Mechanics,” Opt. Eng., **22**(6), p. 226738.

[21] Peters, W. H., and Ranson, W. F., 1982, “Digital Imaging Techniques in Experimental Stress Analysis,” Opt. Eng., **21**(3), p. 213427.

[22] Schreier, H. W., 2003, *Investigation of Two and Three-Dimensional Image Correlation Techniques with Applications in Experimental Mechanics*, University of South Carolina.

[23] Pan, B., Qian, K., Xie, H., and Asundi, A., 2009, “Two-Dimensional Digital Image Correlation for in-Plane Displacement and Strain Measurement: A Review,” Meas. Sci. Technol., **20**(6), p. 062001.

[24] Garcia, D., Orteu, J.-J., and Penazzi, L., 2002, “A Combined Temporal Tracking and Stereo-Correlation Technique for Accurate Measurement of 3D Displacements: Application to Sheet Metal Forming,” J. Mater. Process. Technol., **125**, pp. 736–742.

[25] Pan, B., Xie, H., Yang, L., and Wang, Z., 2009, "Accurate Measurement of Satellite Antenna Surface Using 3D Digital Image Correlation Technique," Strain, **45**(2), pp. 194–200.

[26] Bay, B. K., Smith, T. S., Fyhrie, D. P., and Saad, M., 1999, "Digital Volume Correlation: Three-Dimensional Strain Mapping Using X-Ray Tomography," Exp. Mech., **39**(3), pp. 217–226.

[27] Cooreman, S., Lecompte, D., Sol, H., Vantomme, J., and Debruyne, D., 2008, "Identification of Mechanical Material Behavior through Inverse Modeling and DIC," Exp. Mech., **48**(4), pp. 421–433.

[28] Avril, S., Bonnet, M., Bretelle, A.-S., Grédiac, M., Hild, F., Ienny, P., Latourte, F., Lemosse, D., Pagano, S., and Pagnacco, E., 2008, "Overview of Identification Methods of Mechanical Parameters Based on Full-Field Measurements," Exp. Mech., **48**(4), pp. 381–402.

[29] Springmann, M., and Kuna, M., 2003, "Identification of Material Parameters of the Rousselier Model by Non-Linear Optimization," Comput. Mater. Sci., **26**, pp. 202–209.

[30] Kauer, M., Vuskovic, V., Dual, J., Székely, G., and Bajka, M., 2002, "Inverse Finite Element Characterization of Soft Tissues," Med. Image Anal., **6**(3), pp. 275–287.

[31] Martins, J. M. P., Andrade-Campos, A., and Thuillier, S., 2018, "Comparison of Inverse Identification Strategies for Constitutive Mechanical Models Using Full-Field Measurements," Int. J. Mech. Sci., **145**, pp. 330–345.

[32] Wang, J., Qin, Q. H., Kang, Y. L., Li, X.-Q., and Rong, Q. Q., 2010, "Viscoelastic Adhesive Interfacial Model and Experimental Characterization for Interfacial Parameters," Mech. Mater., **42**(5), pp. 537–547.

[33] Fedele, R., Raka, B., Hild, F., and Roux, S., 2009, "Identification of Adhesive Properties in GLARE Assemblies Using Digital Image Correlation," J. Mech. Phys. Solids, **57**(7), pp. 1003–1016.

[34] Rahmani, B., 2014, "In-Situ Mechanical Properties Identification of Composite Materials Using Inverse Methods Based on Full-Field Measurements," PhD Thesis, École Polytechnique de Montréal.

[35] Ladeveze, P., and Leguillon, D., 1983, "Error Estimate Procedure in the Finite Element Method and Applications," SIAM J. Numer. Anal., **20**(3), pp. 485–509.

[36] Florentin, E., and Lubineau, G., 2011, "Using Constitutive Equation Gap Method for Identification of Elastic Material Parameters: Technical Insights and Illustrations," Int. J. Interact. Des. Manuf. IJIDeM, **5**(4), pp. 227–234.

[37] Guchhait, S., and Banerjee, B., 2016, "Anisotropic Linear Elastic Parameter Estimation Using Error in the Constitutive Equation Functional," Proc. R. Soc. Math. Phys. Eng. Sci., **472**(2192), p. 20160213.

[38] Latourte, F., Chrysochoos, A., Pagano, S., and Wattrisse, B., 2008, "Elastoplastic Behavior Identification for Heterogeneous Loadings and Materials," Exp. Mech., **48**(4), pp. 435–449.

[39] Merzouki, T., Nouri, H., and Roger, F., 2014, "Direct Identification of Nonlinear Damage Behavior of Composite Materials Using the Constitutive Equation Gap Method," Int. J. Mech. Sci., **89**, pp. 487–499.

[40] Grédiac, M., Auslender, F., and Pierron, F., 2001, "Applying the Virtual Fields Method to Determine the Through-Thickness Moduli of Thick Composites with a Nonlinear Shear Response," Compos. Part Appl. Sci. Manuf., **32**(12), pp. 1713–1725.

[41] Moulart, R., Avril, S., and Pierron, F., 2006, "Identification of the Through-Thickness Rigidities of a Thick Laminated Composite Tube," Compos. Part Appl. Sci. Manuf., **37**(2), pp. 326–336.

[42] Toussaint, E., Grédiac, M., and Pierron, F., 2006, "The Virtual Fields Method with Piecewise Virtual Fields," Int. J. Mech. Sci., **48**(3), pp. 256–264.

[43] Promma, N., Raka, B., Grediac, M., Toussaint, E., Le Cam, J.-B., Balandraud, X., and Hild, F., 2009, "Application of the Virtual Fields Method to Mechanical Characterization of Elastomeric Materials," Int. J. Solids Struct., **46**(3–4), pp. 698–715.

[44] Roewer-Despres, F., Khan, N., and Stavness, I., 2018, "Towards Finite Element Simulation Using Deep Learning," *15th International Symposium on Computer Methods in Biomechanics and Biomedical Engineering*.

[45] Tonutti, M., Gras, G., and Yang, G.-Z., 2017, "A Machine Learning Approach for Real-Time Modelling of Tissue Deformation in Image-Guided Neurosurgery," Artif. Intell. Med., **80**, pp. 39–47.

[46] Lorente, D., Martínez-Martínez, F., Rupérez, M. J., Lago, M. A., Martínez-Sober, M., Escandell-Montero, P., Martínez-Martínez, J. M., Martínez-Sanchis, S., Serrano-López, A. J., and Monserrat, C., 2017, "A Framework for Modelling the Biomechanical Behaviour of the Human Liver during Breathing in Real Time Using Machine Learning," Expert Syst. Appl., **71**, pp. 342–357.

[47] Mendizabal, A., Márquez-Neila, P., and Cotin, S., 2020, "Simulation of Hyperelastic Materials in Real-Time Using Deep Learning," Med. Image Anal., **59**, p. 101569.

[48] Wang, M., Dutta, D., Kim, K., and Brigham, J. C., 2015, "A Computationally Efficient Approach for Inverse Material Characterization Combining Gappy POD with Direct Inversion," Comput. Methods Appl. Mech. Eng., **286**, pp. 373–393.

[49] Ghaboussi, J., Garrett Jr, J. H., and Wu, X., 1991, "Knowledge-Based Modeling of Material Behavior with Neural Networks," J. Eng. Mech., **117**(1), pp. 132–153.

[50] Wadham-Gagnon, M., 2006, "Hyperelastic Modelling of Rubber Behaviour in Finite Element Software."

[51] Mooney, M., 1940, "A Theory of Large Elastic Deformation," J. Appl. Phys., **11**(9), pp. 582–592.

[52] Rivlin, Rs., 1948, "Large Elastic Deformations of Isotropic Materials. I. Fundamental Concepts," Philos. Trans. R. Soc. Lond. Ser. Math. Phys. Sci., **240**(822), pp. 459–490.

[53] Yeoh, O. H., 1993, "Some Forms of the Strain Energy Function for Rubber," Rubber Chem. Technol., **66**(5), pp. 754–771.

[54] Shahzad, M., Kamran, A., Siddiqui, M. Z., and Farhan, M., 2015, "Mechanical Characterization and FE Modelling of a Hyperelastic Material," Mater. Res., **18**, pp. 918–924.

[55] Ogden, R. W., 1972, "Large Deformation Isotropic Elasticity–on the Correlation of Theory and Experiment for Incompressible Rubberlike Solids," Proc. R. Soc. Lond. Math. Phys. Sci., **326**(1567), pp. 565–584.

[56] Arruda, E. M., and Boyce, M. C., 1993, "A Three-Dimensional Constitutive Model for the Large Stretch Behavior of Rubber Elastic Materials," J. Mech. Phys. Solids, **41**(2), pp. 389–412.

[57] Carlescu, V., Prisacaru, G., and Olaru, D., 2014, "FEM Simulation on Uniaxial Tension of Hyperelastic Elastomers," *Applied Mechanics and Materials*, Trans Tech Publ, pp. 57–62.

[58] Ribeiro, J. E., Lopes, H., Martins, P., and Braz-César, M. T., 2019, "Mechanical Analysis of PDMS Material Using Biaxial Test," AIMS Mater. Sci., **6**(1), pp. 97–110.

[59] Kim, T. K., Kim, J. K., and Jeong, O. C., 2011, "Measurement of Nonlinear Mechanical Properties of PDMS Elastomer," Microelectron. Eng., **88**(8), pp. 1982–1985.

[60] Tobajas, R., Ibartz, E., and Gracia, L., 2016, "A Comparative Study of Hyperelastic Constitutive Models to Characterize the Behavior of a Polymer Used in Automotive Engines," *Proceedings of the 2nd International Electronic Conference on Materials*, p. A002.

[61] Esmail, J. F., Mohamedmeki, M. Z., and Ajeel, A. E., 2020, "Using the Uniaxial Tension Test to Satisfy the Hyperelastic Material Simulation in ABAQUS," *IOP Conference Series: Materials Science and Engineering*, IOP Publishing, p. 012065.

[62] Martins, P., Natal Jorge, R. M., and Ferreira, A. J. M., 2006, "A Comparative Study of Several Material Models for Prediction of Hyperelastic Properties: Application to Silicone-Rubber and Soft Tissues," Strain, **42**(3), pp. 135–147.

[63] Liu, C., Cady, C. M., Lovato, M. L., and Orler, E. B., 2015, "Uniaxial Tension of Thin Rubber Liner Sheets and Hyperelastic Model Investigation," J. Mater. Sci., **50**(3), pp. 1401–1411.

[64] Thanakhun, K., and Puttapitukporn, T., 2019, "PDMS Material Models for Anti-Fouling Surfaces Using Finite Element Method," Eng. J., **23**(6), pp. 381–398.

[65] Huri, D., and Mankovits, T., 2018, "Comparison of the Material Models in Rubber Finite Element Analysis," *IOP Conference Series: Materials Science and Engineering*, IOP Publishing, p. 012018.

[66] Mata, A., Fleischman, A. J., and Roy, S., 2005, "Characterization of Polydimethylsiloxane (PDMS) Properties for Biomedical Micro/Nanosystems," Biomed. Microdevices, **7**(4), pp. 281–293.

[67] Bernardi, L., Hopf, R., Ferrari, A., Ehret, A. E., and Mazza, E., 2017, "On the Large Strain Deformation Behavior of Silicone-Based Elastomers for Biomedical Applications," Polym. Test., **58**, pp. 189–198.

[68] Khanafer, K., Duprey, A., Schlicht, M., and Berguer, R., 2009, "Effects of Strain Rate, Mixing Ratio, and Stress–Strain Definition on the Mechanical Behavior of the Polydimethylsiloxane (PDMS) Material as Related to Its Biological Applications," Biomed. Microdevices, **11**(2), pp. 503–508.

[69] Johnston, I. D., McCluskey, D. K., Tan, C. K. L., and Tracey, M. C., 2014, "Mechanical Characterization of Bulk Sylgard 184 for Microfluidics and Microengineering," J. Micromechanics Microengineering, **24**(3), p. 035017.

[70] Pan, B., 2018, "Digital Image Correlation for Surface Deformation Measurement: Historical Developments, Recent Advances and Future Goals," Meas. Sci. Technol., **29**(8), p. 082001.

[71] Pan, B., Lu, Z., and Xie, H., 2010, “Mean Intensity Gradient: An Effective Global Parameter for Quality Assessment of the Speckle Patterns Used in Digital Image Correlation,” Opt. Lasers Eng., **48**(4), pp. 469–477.

[72] Lecompte, D., Smits, A., Bossuyt, S., Sol, H., Vantomme, J., Van Hemelrijck, D., and Habraken, A. M., 2006, “Quality Assessment of Speckle Patterns for Digital Image Correlation,” Opt. Lasers Eng., **44**(11), pp. 1132–1145.

[73] Yazdi, A. A., Melchor, J., Torres, J., Faris, I., Callejas, A., Gonzalez-Andrades, M., and Rus, G., 2020, “Characterization of Non-Linear Mechanical Behavior of the Cornea,” Sci. Rep., **10**(1), pp. 1–10.

[74] Humphrey, J. D., 2013, *Cardiovascular Solid Mechanics: Cells, Tissues, and Organs*, Springer Science & Business Media.

[75] Ogden, R. W., Saccomandi, G., and Sgura, I., 2004, “Fitting Hyperelastic Models to Experimental Data,” Comput. Mech., **34**(6), pp. 484–502.

[76] Keerthiwansa, G. W. R., Javořík, J., Kledrowetz, J., and Nekoksa, P., 2018, “Elastomer Testing: The Risk of Using Only Uniaxial Data for Fitting the Mooney-Rivlin Hyperelastic-Material Model,” Mater. Tehnol.

[77] He, H., Zhou, R., Zou, Y., Huang, X., and Li, J., 2018, “A Comprehensive Method for Accurate Strain Distribution Measurement of Cell Substrate Subjected to Large Deformation,” J. Healthc. Eng., **2018**.

VITA

S. M. Rakibur Rahman

Candidate for the Degree of

Master of Science

Thesis: MECHANICAL CHARACTERIZATION OF HETEROGENEOUS HYPERELASTIC MEMBRANE USING INVERSE METHODS

Major Field: Mechanical and Aerospace Engineering

Biographical:

Education:

Completed the requirements for the Master of Science in Mechanical and Aerospace Engineering at Oklahoma State University, Stillwater, Oklahoma in December, 2021.

Completed the requirements for the Bachelor of Science in Aeronautical Engineering at Bangladesh University of Professionals, Dhaka, Bangladesh in 2017.

Experience:

Graduate Research Assistant, Mechanics and Materials Laboratory, Oklahoma State University (June 2020- December 2021).

Graduate Teaching Assistant, Oklahoma State University (August 2019-May 2020, August 2021-December 2021).